

Cooling and optimizing urban heat island based on a thermal knowledge-informed multi-type ant colony model

Zhaomin Tong^a, Jiaming Yang^a, Yaolin Liu^{a,b,*}, Ziyi Zhang^c, Sui Liu^a, Yanchi Lu^a, Bowen Pang^a, Rui An^a

^a School of Resource and Environmental Sciences, Wuhan University, Wuhan 430079, China

^b Duke Kunshan University, Kunshan 215316, China

^c School of Surveying and Geoinformation Engineering, East China University of Technology, Nanchang 330013, China



ARTICLE INFO

Edited by Jing M. Chen

Keywords:

Urban heat island
Inverse S-shaped function
Land use optimization
Cooling effect

ABSTRACT

In the context of rapid urbanization and global warming, the urban heat island (UHI) intensifies the risk of heat-related mortality, endangering the health of urban residents. Urban greening effectively mitigates severe urban heating climates, but increasing green space without restrictions is undesirable due to the scarcity of urban land. Accurately characterizing the scope and intensity of UHI and determining the spatial location of the area that needs to be optimized are necessary. In this study, an inverse S-shaped function was used to fit the urban-rural temperature attenuation, whose parameters explicitly describe the properties of UHI. Additionally, a thermal knowledge-informed multi-type ant colony model was proposed to cool UHI automatically. A case study of Wuhan showed that: (1) the fitting effect of the inverse S-shaped function is desirable with the adjusted R^2 exceeding 0.97, and the derived parameters with clear physical meanings avoid subjectivity in describing thermal characteristics; (2) high-level heat island of the main urban areas can be reduced by 7.7%–8.5% after land use optimization; and (3) a comparison with the traditional multi-type ant colony model verifies that the model proposed in this study can avoid excessive dispersion of the optimized pixels whose land use types are modified and achieve more reasonable and stable optimization results. This study provides useful exploratory tools for sustainable urban planning, heat mitigation solutions, and other urban retrofitting.

1. Introduction

UN-Habitat pointed out in the World Cities Report 2022 that the growth of the global urban population is returning to the track of rapid growth after suffering from the global COVID-19 pandemic (UN-Habitat, 2022). Moreover, the proportion of the global urban population is expected to increase from 56% in 2021 to 68% by 2050 (<https://unhabitat.org/cn>). Under the background of rapid and drastic urbanization, the transformation of natural green space into impervious surface in urban areas has been considerably accelerated, resulting in the urban heat island (UHI) effect (Liao et al., 2021; Meng et al., 2018; Wang et al., 2021b). UHI is characterized by higher land surface temperatures (LSTs) in urban areas than in rural areas, and it has caused a wide range of negative impacts, including extreme weather events, biodiversity reduction, increased energy consumption and health problems among urban dwellers (Schwarz et al., 2011). In 2022, extreme high-temperature weather frequently occurred worldwide during summer,

and the highest temperature in many countries broke historical records. The China Climate Bulletin 2022 indicated that in the summer of 2022, the average number of high-temperature days in China was 3.6 days more than the same period in previous years, i.e., the greatest in history since 1961, and the highest temperatures in 131 national meteorological stations reached or exceeded the historical extreme values (National Climate Center of China Meteorological Administration, 2022). Therefore, governments and urban planners are urgently finding solutions to curb the growing heat in cities. Urban ecological land (UEL), a combination of green space or semi-natural ecosystems, can introduce significant cooling effects (Feng et al., 2021). Optimizing the spatial layout of UEL has been proven to be an effective strategy to curb urban high temperatures at the city level (Peng et al., 2021). Therefore, accurately quantifying UHI and formulating reasonable UEL planning in urban main built-up areas (UMBA), i.e., urban areas with highly concentrated impermeable surfaces, is crucial for improving the urban thermal environment and creating eco-friendly and sustainable urban regions.

* Corresponding author at: School of Resource and Environmental Sciences, Wuhan University, Wuhan 430079, China.

E-mail address: yaolin610@yeah.net (Y. Liu).

In UHI research, surface urban heat island (SUHI) has received extensive attention due to the easy access and high spatio-temporal resolution of remote sensing data (Shen et al., 2016). In addition, SUHI has broader applicability and larger spatial extent compared with air temperature-based UHI, which only captures site-level atmospheric temperature difference (Qian et al., 2023; Xue et al., 2022). Meanwhile, SUHI is also closely related to residents' daily life and environmental health within urbanized regions. Therefore, studying SUHI based on LST thus has become increasingly popular in the field of urban thermal environment (Wang et al., 2023). SUHI intensity has been reported to be higher at night due to the differences in heat dissipation between urban and rural areas (Possega et al., 2022). While considering the frequency of human outdoor activities and the availability of nocturnal data, more studies on daytime SUHI have been conducted to guide UEL planning. SUHI intensity is commonly used to measure the degree of temperature difference between urban and rural areas (Zhou et al., 2022). Focusing on SUHI intensity is not only a recognition of the potential risk of regional high-temperature heat but also a quantitative analysis research premise for the effectiveness of mitigation measures for the SUHI effect. Various methods for measuring SUHI intensity have been proposed, such as the Gaussian surface model (Yao et al., 2022), urban-rural temperature difference (Mohammad and Goswami, 2022), LST magnitude (Nguyen et al., 2022), and surface temperature difference between cities and water surfaces (Welegedara et al., 2023). Schwarz et al. (2011) compared the 11 most commonly used quantitative indicators for SUHI intensity and found a weak correlation although they theoretically quantified the same phenomenon. Among these indicators, the LST difference between urban and rural areas has been widely regarded as the most commonly used indicator for SUHI intensity, in accordance with a literature review (Deilami et al., 2018). However, the definition of the rural background remains problematic. Yao et al. (2022) used 31 cities in China as the research objects; compared the SUHI intensity under different definition methods for rural backgrounds; and found that the SUHI intensity differed based on seasonal characteristics, interannual changes, and spatial distributions. In SUHI intensity-computing research, buffer ranges, elevation influences, and land use coverage are regarded as major factors influencing SUHI intensity definition at the regional scales (Wang et al., 2021b; Zhou et al., 2022).

The two major categories of methods for delineating the background references are boundary-based and temperature mutation-based (Li et al., 2022a; Yao et al., 2018). Boundary-based methods mainly delimit the boundaries between urban and rural areas, including buffer zone boundaries, urban administrative boundaries, urban land cover, and other land types or regions around weather stations in cities and rural areas (Li et al., 2019; Sugg et al., 2022). Although boundary-based methods have been extensively applied in previous research because of their simplicity and efficiency, Li et al. (2022a) reported that the accuracy of boundary delimitation brought uncertainty to spatiotemporal variations in SUHI intensity. In terms of urban boundary selection, many studies have used the average temperature of the entire urban built-up area to calculate the SUHI intensity, while some studies have only selected several pixels of the urban core area as the representative of urban temperature (Meng et al., 2018; Walawender et al., 2013). When UMBA cannot be effectively extracted, accurately determining the scope and intensity of the SUHI effect is difficult. With regard to the definition of the rural background area, most studies have selected the average temperature of the buffer zone outside the urban built-up area as the rural background temperature, where the area of the buffer zone was the same as that of the urban area, or the width of the buffer zone was manually set (Deng et al., 2023; Jain et al., 2020). However, Zhou et al. (2022) suggested that the buffer zone adjacent to the urban built-up area belongs to the suburb, not rural area, which is likely to be within the scope of SUHI, and that the method may underestimate SUHI intensity. In addition, for cities with high economic levels, relatively concentrated human activities may occur in the surrounding rural areas, resulting in small-scale UHI (Athukorala and Murayama, 2021). To

overcome the limitations of urban-rural division, particularly the definition of rural background areas, scholars have proposed temperature mutation-based methods for measuring SUHI intensity. Qiao et al. (2019) developed an algorithm for measuring the trend of LST decay from urban to rural areas based on a logistic curve and the temperature of rural reference background corresponding to the LST mutation value in the fitting curve. Athukorala and Murayama (2021) found the LST breakpoint along the direction of urban-rural gradient circle and used it as background temperature. Xue et al. (2022) proposed the concentric zone model, which depicted the urban-rural spatial structure in accordance with different LST decline rates. In addition, Li et al. (2018) fitted the LST and impervious surface area based on the linear equation and measured SUHI intensity by using the slope of the fitting equation. Chakraborty et al. (2020) proposed a simplified SUHI intensity calculation method that does not define urban-rural buffer zones. The aforementioned studies avoid the division of urban-rural boundaries and improve the accuracy and reliability of background temperature. However, the determination of the temperature mutation point (or breakpoint) of the LST decay curve is typically human-dominated, and the parameters in the fitting function do not have a clear physical meaning under the UHI background. In addition, generating the scope of SUHI by using temperature-mutation-based methods is difficult because of the lack of built-up area boundaries.

In addition to the range, intensity, spatio-temporal distribution, and influencing factors of SUHI, how to cool the identified SUHI is also an important issue (Chen et al., 2022; Sheng et al., 2022; Yu et al., 2020). Urban greenery in heat has been proven to be a feasible mitigation method with additional social and ecological benefits at the city level (Rakoto et al., 2021). However, determining the number and spatial position of added green spaces to improve the cooling effect poses a difficult problem to researchers. Some studies have simulated the physical process of heat exchange in the building environment based on the urban system dynamics or physical thermal models to optimize the urban green space design scene and obtain the ideal urban mitigation effect (Li et al., 2022b; Pena Acosta et al., 2021). Although physical-based urban land surface models enable a relatively accurate assessment effect, calculation time consumption remains costly, and guiding the city-wide greening strategy is difficult. Spatial land use allocation exhibits good agreement with multi-objective nonlinear optimization (Kaim et al., 2018; Rahman and Szabó, 2021). Bionic intelligent optimization algorithms, such as ant colony optimization (ACO) (Wang et al., 2021a), genetic algorithms (GA) (Li and Parrott, 2016), and particle swarm optimization (PSO) algorithms (Liu et al., 2016), exhibit good performance in solving the spatial optimization of land use resources. In the field of UHI mitigation, (Zhang et al., 2021) proposed an improved multi-type ant colony algorithm for locating and cooling an urban heat core and provided a scientific basis for urban ecological retrofits. However, studies based on optimization algorithms have given more attention to surface features and regard them as the suitability of different land types, disregarding the synthetic characteristics of urban dynamics. Thus, the comprehensive consideration of urban form, surface feature combinations, and population distribution is essential to formulate specific regional strategies and further understand the environmental response under possible scenarios. Additionally, integration of the intensity and spatial distribution of SUHI into the iterative process can encourage the algorithm to increase its attention to areas that require urgent cooling.

To address the aforementioned issues, this study uses Wuhan as an example, identifies the scope of SUHIs, and delimits the different heat island grades. Based on the improved multi-type ant colony optimization (MACO) algorithm, the spatial location of the pixel is optimized by comprehensively considering a combination of land surface features, population distribution, and SUHI intensity to alleviate the UHI effect at the city level. The following questions are tried to be answered. (1) How can manual interference be avoided in the fitting of background temperature? (2) How can land use distribution for large-area images with

higher spatial resolution be optimized under the dynamic adjustment of land use type and quantity? (3) How can the identified SUHI information be integrated into the model and endow the ants in the MACO algorithm with the ability to perceive the thermal environment?

The main contributions of this study are as follows. (1) An urban-rural LST attenuation fitting method, the parameters of which have clear physical meanings, was applied to avoid subjectivity in determining rural background temperature. (2) The boundary delimitation of the built-up area and the fitting of background temperature were integrated to consider the intensity and scope of SUHI comprehensively. (3) An improved MACO algorithm for SUHI cooling was proposed, which endows ants with the ability to perceive their thermal attributes, evaluate the surrounding thermal environment, and identify the urban population aggregation and SUHI core areas. Under the premise of minimizing change in the current land use status, the proposed algorithm can adjust and optimize land use distribution with high spatial resolution at the city level, considering the multi-dimensional characteristics of the city, thereby reducing the urban surface temperature and alleviating the SUHI effect.

2. Study area and dataset

2.1. Study area

We choose Wuhan, which is located within $113^{\circ}41' - 115^{\circ}05'$ E and $29^{\circ}58' - 31^{\circ}22'$ N, as the study area (Fig. 1). Wuhan is the core city in central China, having a total area of 8569.15 km² and a resident population of >13.6 million by the end of 2022. It is located in the transition zone from the southeast hills of Hubei to the Dabie Mountains, which is low and flat in the middle, and hilly in the north and south. The altitude

of Wuhan ranges from 19 m–870 m above sea level, and most of the central area is below 50 m. As China's largest foreign exchange center, Wuhan has held many large-scale international events in the past few years, such as the 7th International Military Sports Council Military World Games and the International Horse Race Festival. With the rapid expansion of built-up areas in Wuhan, problems related to the SUHI effect are becoming increasingly serious. Wuhan belongs to the subtropical monsoon climate zone, which is characterized by hot summers and short springs and autumns. Due to the high temperature of summer, Wuhan is also known as one of China's "furnace cities" (Shen et al., 2016). In the summer of 2022, Wuhan has 33 days of high temperature (daily maximum temperature > 35 °C), ranking first in its history since 1961 during the same period (<https://www.chinanews.com/sh/2022/08-21/9833209.shtml>). Continuous extreme high-temperature weather (daily maximum temperature > 40 °C) occurred in Wuhan, resulting in casualties among outdoor workers. During the August 2022 heat wave event in Wuhan, over 90 people suffered from heatstroke and meteorological droughts occurred in many farmland areas, seriously threatening the lives and properties of residents. Therefore, studying the spatial distribution and mitigation measures of SUHI is necessary to promote urban sustainable development.

2.2. Data collection

The UMBA and LST were extracted from the Landsat-8 image. The Landsat-8 satellite carries two science instruments: the Operational Land Imager (OLI) and the Thermal Infrared Sensor (TIRS), which the sensors improve the overall signal-to-noise ratio and allow better accuracy of land cover classification and characterization. The specifications and parameters of Landsat-8 products can be acquired in the NASA/USGS

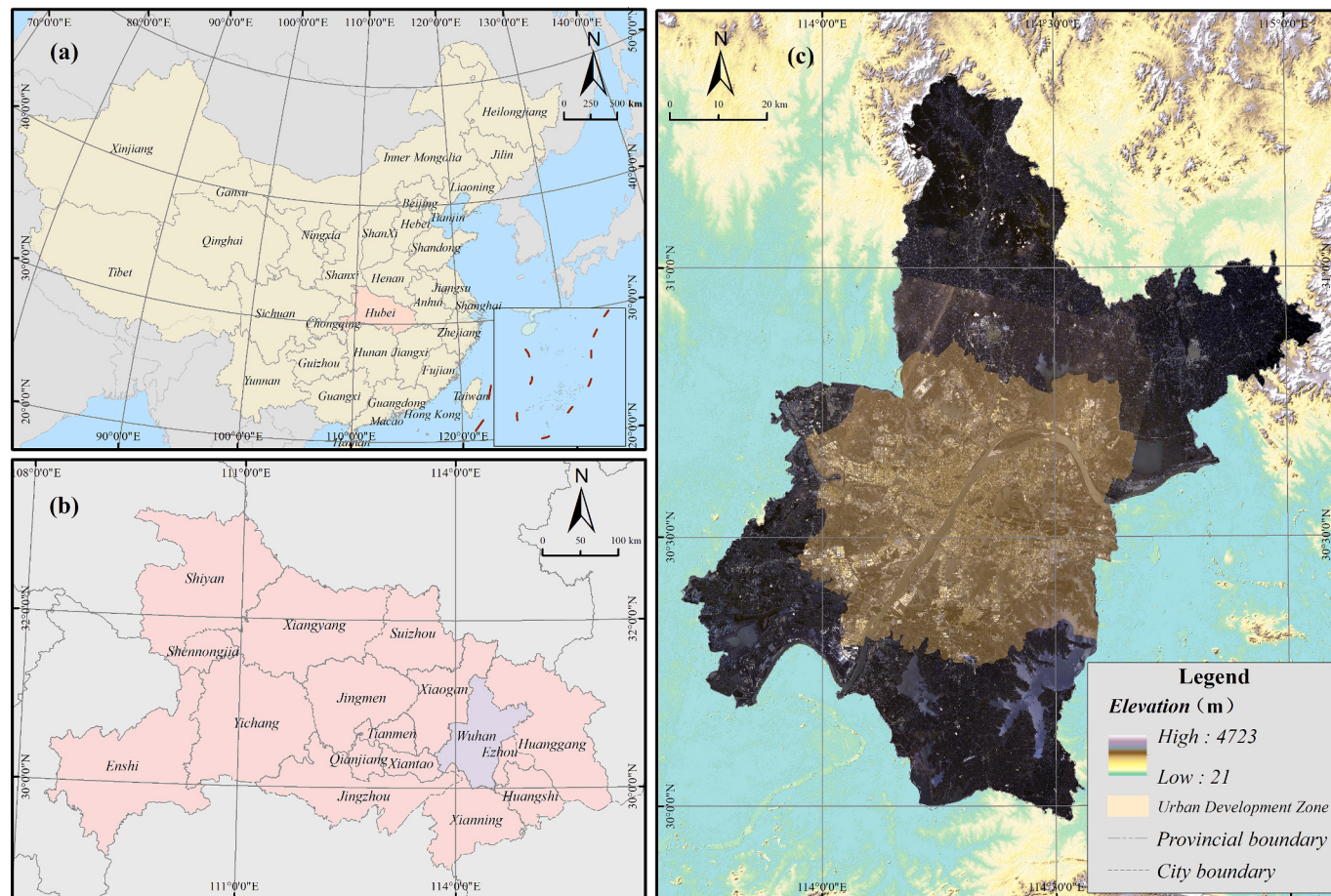


Fig. 1. Administrative divisions and remote sensing image of Wuhan from August 2022.

Landsat Program (<https://landsat.gsfc.nasa.gov/landsat-8>).

This study collected Landsat-8 images on August 3, 2016, and August 3, 2022, from USGS web (<https://glovis.usgs.gov/app>). The weather in Wuhan on the selected date is fine and cloudless, without special events, and the average temperature is between 28 and 39 °C. After seamless mosaic and clipping using administrative region, the study area consists of 9,547,501 cells (5276 rows and 4567 columns) of 30 × 30 m. Besides, we used the Digital Elevation Model (DEM) data (<http://www.gscloud.cn/>), land use cover classification data (<http://www.globallandcover.com/>), and user density data collected from Baidu, the biggest Internet company in China with numerous active users (<https://huiyan.baidu.com/products/platform>). The proportion of Baidu users among smartphone users in China has exceeded 80% and Baidu user density (BUD) data have been widely applied to depict real-time regional vitality and resident dynamics (Tong et al., 2022; Zhang et al., 2022). The real-time locations of mobile devices with installed applications provided by Baidu are recorded by base stations when these applications are used or running in the background. Each base station can be regarded as a recording point, which records the number of Baidu users within its service range at a certain time. We collected Baidu user spatial distribution data during daytime (7:00–22:00) in August 2021, with 52,525 base stations recording an average daily distribution of 3,521,467 users in the Wuhan Urban Development Zone. By rasterizing and averaging the spatial distribution of Baidu users recorded by the base stations in August, we obtained the BUD data used in this study (Fig. 2). All data were resampled to 30 m spatial resolution and those websites were accessible on 20 March 2023.

3. Methods

The method was mainly divided into two parts: SUHI identification and SUHI cooling. First, based on the biophysical composition index (BCI) and impervious surface distribution density (ISDD), the UMBA boundary was extracted using a city clustering algorithm (CCA). After LST retrieval, a new method was used to obtain the rural background temperature based on an inverse S-shaped function, and the parameters of the function had specific physical meanings. The SUHI intensity level was determined by comparing the LST differences between the urban and rural areas. Finally, a novel MACO algorithm coupled with multi-dimensional environmental perception was developed to realize SUHI

cooling. A flowchart of the method used in this study is shown in Fig. 3:

3.1. SUHI identification

3.1.1. Boundary of UMBA extraction

Accurately extracting the boundary of urban areas is crucial for determining the impact scope of SUHI, which can be achieved through two steps of ISDD calculation and city clustering algorithm. BCI, an index based on the vegetation–impervious surface–soil (V–I–S) model, is generally used to characterize urban impervious surfaces (Deng and Wu, 2012). Similar to principal component analysis (PCA), tasseled cap (TC) transformation projects the original image to the three-dimensional feature space of the feature vectors of brightness (TC1), greenness (TC2), and humidity (TC3) with physical meanings in accordance with a fixed transformation matrix, which is equivalent to classifying the albedo of different land cover types. Particularly, TC1 and TC3 are highly related to impervious surfaces through spectral analysis (Deng and Wu, 2012; Wang et al., 2022b). After water masking and reexamination of TC transformation based on Landsat-8 images, BCI can be given by the following formula:

$$BCI = \frac{(H + L)/2 - V}{(H + L)/2 + V} \quad (1)$$

where H refers to the normalized TC1 or “high albedo”; L represents normalized TC3 or “low albedo”; V represents normalized TC2 or “vegetation”. These three factors can be described as the following formula:

$$H = \frac{TC1 - TC1_{min}}{TC1_{max} - TC1_{min}} \quad (2)$$

$$V = \frac{TC2 - TC2_{min}}{TC2_{max} - TC2_{min}} \quad (3)$$

$$L = \frac{TC3 - TC3_{min}}{TC3_{max} - TC3_{min}} \quad (4)$$

where TCi ($i=1, 2$, and 3) is the first three TC components. TCi_{max} and TCi_{min} are the maximum and minimum values of the i th TC components, respectively. BCI aims to separate bare soil and impervious surfaces, and the higher the BCI value, the greater the probability of land coverage

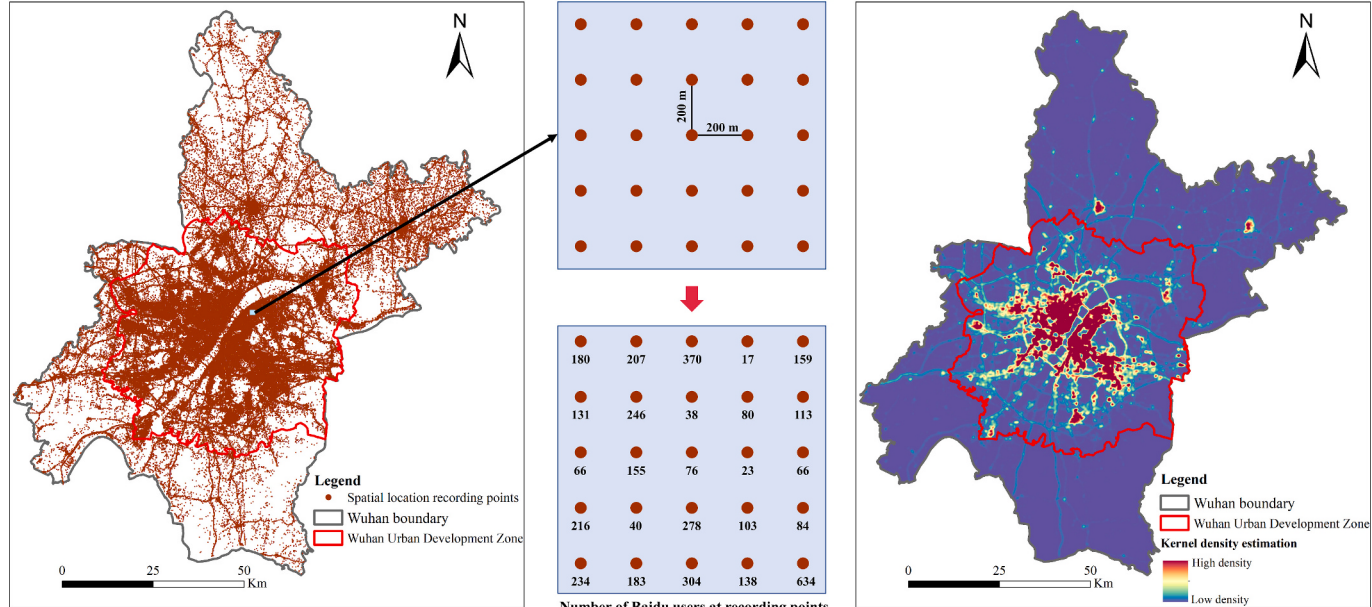


Fig. 2. Schematic diagram and spatial distribution of base station and BUD data.

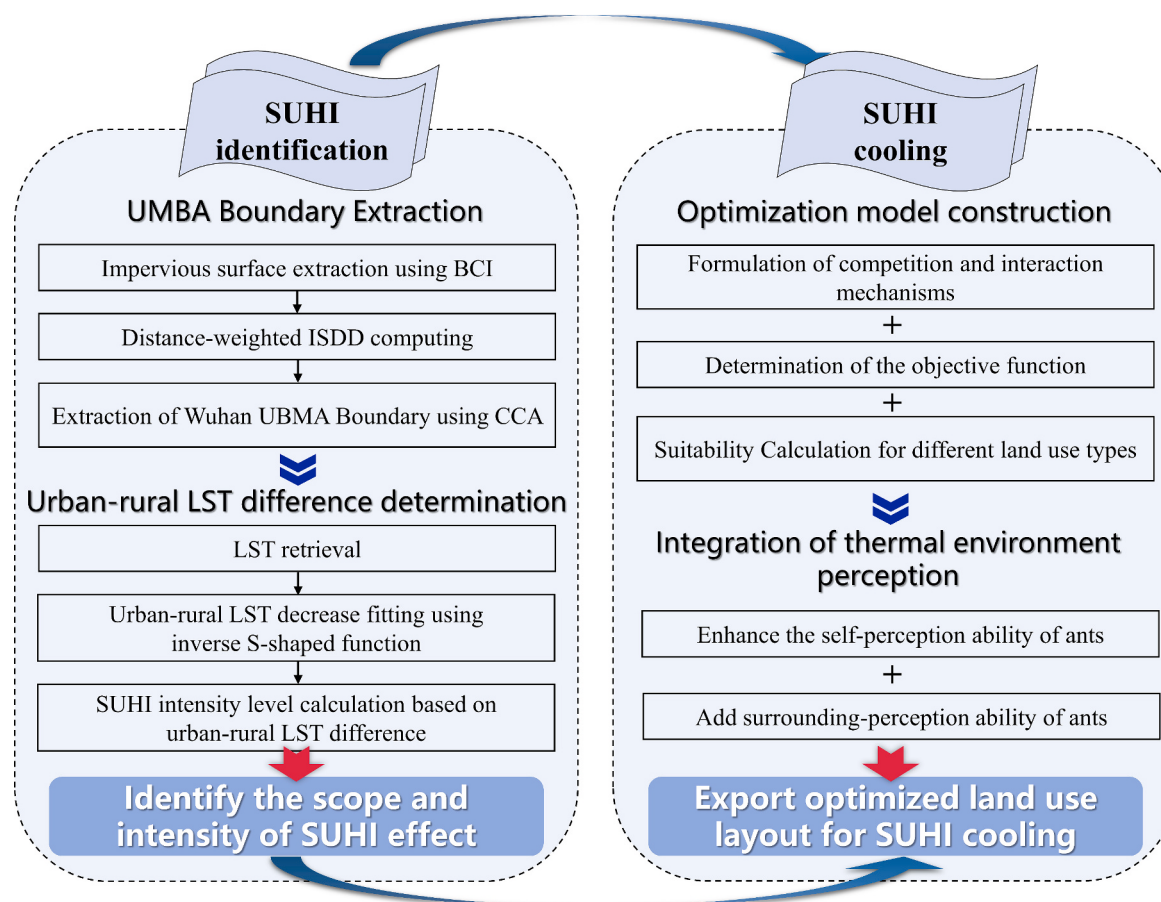


Fig. 3. Implementation framework for the current study.

being impervious surfaces. The threshold value of BCI was set to -0.1 based on visual interpretation to extract impervious surfaces.

After extracting the impervious surfaces, considering the density of impervious surfaces in the main built-up areas is greater than that in the suburbs, the UMBA boundary can be extracted by calculating ISDD and combining the integrity of the underlying surface. The ISDD value of pixels within radius r $\text{Density}_s(r)$ can be calculated as follows (Meng et al., 2018):

$$\text{Density}_s(r) = \frac{\sum_{i=1}^n B_{si} \left(1 - \frac{D_i}{2r}\right)}{\sum_{i=1}^n \left(1 - \frac{D_i}{2r}\right)} \quad (5)$$

where s refers to the central pixel, B_{si} indicates whether the pixel i within radius r is the impervious surface (impervious surface pixel = 1; others = 0), D_i represents the distance from pixel i to the center pixel. The size of the calculation window r reflects the refinement level of the ISDD value. A small value of r can accurately characterize impervious surfaces at a fine scale, but with a high degree of fragmentation, which may be hard to depict the overall distribution; while when r is large, the ISDD patches may become too contiguous to present local detail. After testing multiple values of r (see Supplementary Fig. S1), the calculation window radius of each pixel was set to 1500 m in this study.

The city clustering algorithm was used to measure the integrity of the underlying surface type, which has three steps (Rozenfeld et al., 2008): (1) Select the impervious surface pixels as the central pixel at random, and calculate the connected area of the impervious surface in the Moore neighborhood; (2) define the distance threshold L , and merge the connected areas with a distance less than L ; (3) define the aggregation threshold S , remove the connected area with the number of pixels less

than S , and obtain the distribution of the impervious surface aggregation area. Based on different ISDD inputs, the boundaries of different urban construction density areas can be obtained.

3.1.2. LST retrieval

LST was retrieved using the method proposed by Chen and Zhang (2017), which establishes the functional relationship between land surface cover type and LST. First, the normalized difference vegetative index (NDVI) and modified normalized difference water index (MNDWI) were calculated:

$$\text{NDVI} = \frac{R_{NIR} - R_{RED}}{R_{NIR} + R_{RED}} \quad (6)$$

$$\text{MNDWI} = \frac{R_{GREEN} - R_{MIR}}{R_{GREEN} + R_{MIR}} \quad (7)$$

where R_{NIR} , R_{RED} , R_{GREEN} , and R_{MIR} refer to the reflectance of the near-infrared band, red band, green band, and mid-infrared band of Landsat OLI data, respectively. Second, four types of surface cover including water areas (based on MNDWI), low NDVI areas (LNDVI, such as road, urban, bare land, and industrial district), moderate NDVI areas (MNDVI, such as grassland, sparse vegetation cover regions, and arable land), and high NDVI areas (HNDVI, such as forest and vegetative areas) were classified using k-means clustering method. Specifically, in the example of Wuhan in 2022, the clustering centers of different land types by dividing NDVI are 0.213, 0.474, and 0.695, respectively. To validate the classification accuracy, 200 sample test points were randomly generated within the research area. Based on visual interpretation and taking the high-resolution remote sensing images from Esri's Wayback Living Atlas (https://services.arcgis.com/ArcGIS/rest/services/World_Imager

y/MapServer) as a reference, the average classification accuracy of the four types of surface cover was 81% (Fig. 4a). Then convert the raw digital numbers (DNs) of the thermal infrared band to the blackbody temperature T_b (or brightness temperature):

$$T_b = \frac{K2}{\ln\left(\frac{K1}{L_\lambda} + 1\right)} \quad (8)$$

$$L_\lambda = \text{gain} * DN + \text{offset} \quad (9)$$

where $K1$, $K2$, gain and offset are the calibration constants, which can be found in the Landsat-8 metadata. Specifically, band 10 was selected to retrieve the LST, according to the recommendation of the National Aeronautics and Space Administration (NASA) (Yu et al., 2014). Finally, the emissivity-corrected surface temperature can be calculated (Fig. 4b):

$$T_s = \frac{T_b}{1 + \left(\frac{\lambda \times T_b}{a}\right) \ln e} \quad (10)$$

$$a = \frac{hc}{K} \varepsilon_L \quad (11)$$

$$\varepsilon_{LNDVI} = 0.9608420 + 0.0860322P_V - 0.0671580P_V^2 \quad (12)$$

$$\varepsilon_{MNDVI} = 0.9643744 + 0.0614704P_V - 0.0461286P_V^2 \quad (13)$$

$$\varepsilon_{WATER} = 0.995$$

$$\varepsilon_{HNDVI} = 0.986$$

$$P_V = \frac{NDVI - NDVI_S}{NDVI_V - NDVI_S} \quad (14)$$

where T_s is surface temperature in degrees Kelvin; T_b represents black body temperature in degrees Kelvin; λ represents the emitted radiation wavelength; h is Planck's constant; c is the velocity of light; K is the Boltzmann constant; e is land surface emissivity and different values are taken for different land surface types; P_V is the vegetation proportion estimated from NDVI; $NDVI_V$ and $NDVI_S$ are the NDVI value of the abundant vegetation-covered area and non-vegetation-covered area. Considering that urban built-up areas are the main research object and there are no obvious vegetation-dense or bare soil pixels, the $NDVI_V$ and $NDVI_S$ are assigned 0.7 and 0.05 according to previous studies (Chen and

Zhang, 2017; Yang et al., 2014). In addition, compared with the most widespread algorithm (NDVI Thresholds Method) proposed by Sobrino et al. (2008) (see Supplementary Fig. S2), the method used in this study obtained a larger high-temperature coverage in urban main built-up area, which is more in line with the high value distribution of thermal infrared band (Fig. 4c). The average difference of LST (excluding water body) calculated by the two methods is 0.32 °C and the LST Root Mean Square Error (RMSE) is 0.53 °C, which tested the validity of the method used in the study.

3.1.3. Urban-rural LST decrease fitting

After obtaining the UMBA boundary, determining rural background temperature is necessary to calculate the urban-rural LST difference. Generating a buffer zone or manually searching for a temperature-decay mutation point is subjective. Therefore, based on the inverse S-shaped function, a fitting method without manual interference was applied to determine rural background temperatures.

Scholars have found that variations in geographical elements, such as land density, population density, and facility point density, along the urban-rural gradient tend to exhibit distinct inverse S-shapes (Jiao, 2015; Xu et al., 2019). According to the rate of decline in geographical elements, cities can be divided into regions (i.e., urban core, inner urban zones, urban fringe, and the periphery). Similarly, the attenuation of LST from the urban center to the periphery has been confirmed (Yao et al., 2022). Due to the concentration and dispersion of impermeable surfaces and human activities in different regions, there may also be spatial zoning of urban heat island intensity. The spatial quantitative explicit expression of the attenuation rate, influence range, and other characteristics of UHI is a beneficial exploration combining statistical laws and geographical phenomena. The background temperature of rural areas (or surrounding non UHI areas) is typically considered the temperature that has experienced a sharp decline in urban-rural LST and returned to a stable state again. This variation trend of LST is very close to the shape of the inverse S. Therefore, we attempted to describe spatial variation in LST with a modified inverse S-shaped function, which differs from common curves such as linear, inverse power, and negative exponential functions. First, we determined the center of the city and partitioned the study area using concentric rings. Considering the uneven intensity and direction of urban expansion, we used a ring of equal area instead of equal width and calculated the average LST of each ring (Qiao et al., 2019). Large water bodies and high-altitude regions were subtracted from the total area to avoid possible abnormal fluctuations in average temperature (Fig. 5). Subsequently, the LST can be fitted with the

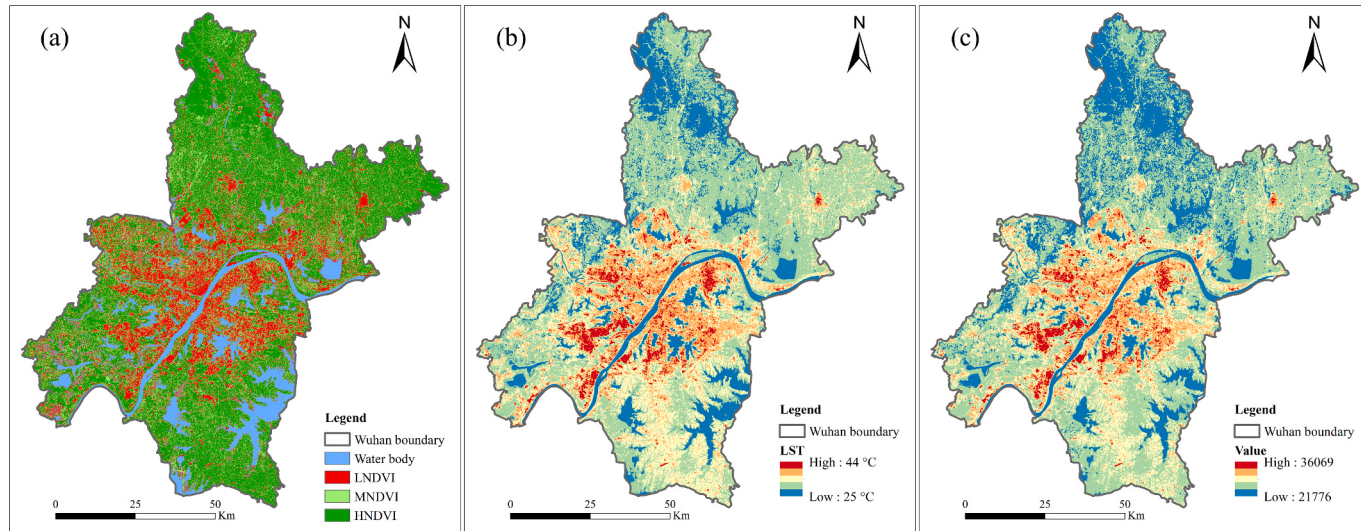


Fig. 4. Spatial distribution of (a) land cover classification by NDVI, (b) LST retrieval result and (c) thermal infrared band value (band 10) from August 2022.

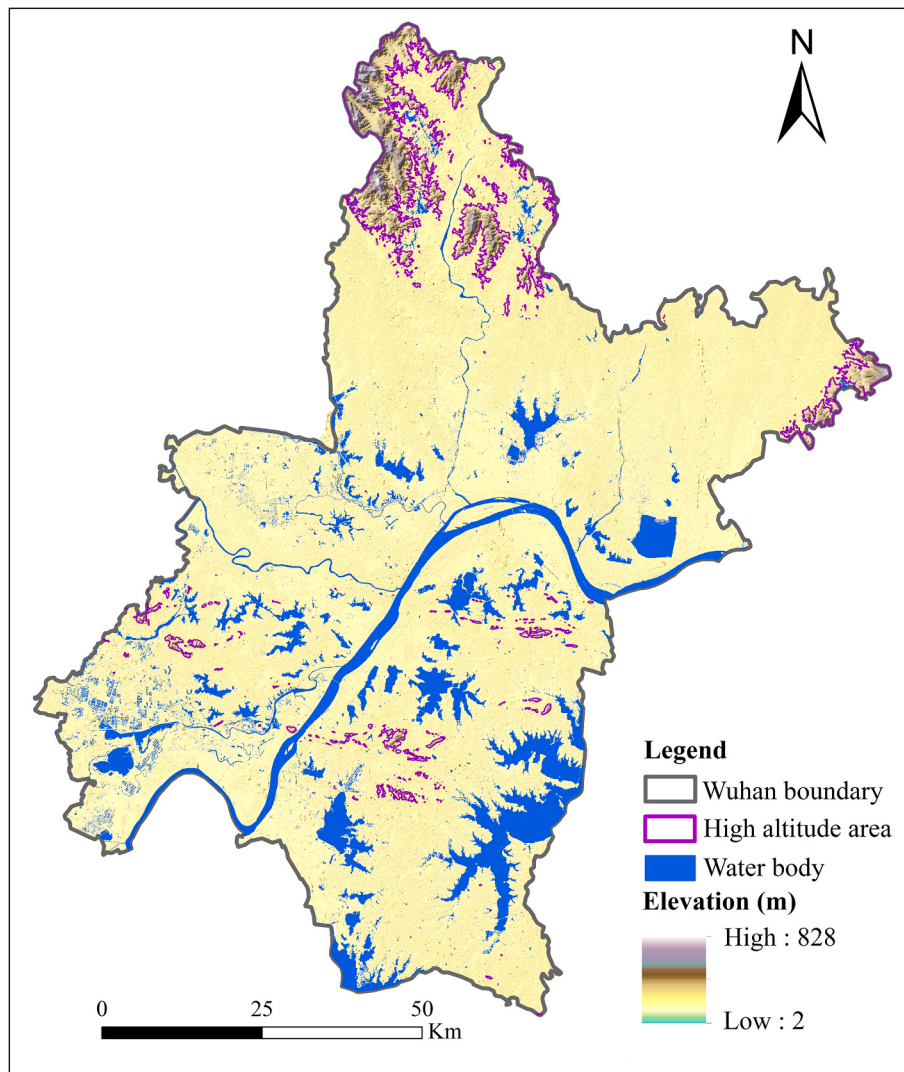


Fig. 5. Water and high-altitude areas excluded from the analysis.

following function:

$$f(r) = \frac{t - c}{1 + e^{a\left(\left(\frac{2r}{D}\right) - 1\right)}} + C \quad (15)$$

where $f(r)$ represents the LST value at ring r ; r is the buffer ring number, indicating the distance to the urban center; and t , c , α , and D are the parameters. This function can be regarded as continuous, monotonically decreasing, or differentiable without considering the discreteness of the rings. A non-linear least squares method based on the trust-region algorithm was used to fit the function, and the parameters denote some urban-rural LST characteristics. Parameters t and c are the two horizontal asymptotes. As r approaches infinity, $f(r)$ approaches c , indicating the average temperature of the hinterland (beyond the scope of urban periphery). As r approaches negative infinity, $f(r)$ approaches t and when $r = 0$ (urban heat core), $f(0) = (t - c)/(1 + e^{-\alpha}) + c$. Considering that α is typically a constant >1.5 (referring to the examples in this study and existing similar research), then $1 + e^{-\alpha}$ will be close to 1 and $f(0)$ will be slightly less than t , which means that parameter t can be used as a reference when comparing average temperatures in different urban heat cores.

The slope of the fitting function is an important manifestation of the inverse S-shaped rule, and different intervals of slope variation also correspond to the spatial partitioning of UHI. To better understand the

decay of LST from the urban core to the periphery, the derivatives of the inverse S-shaped function should be examined. In particular, the first derivative describes the attenuation rate of LST, while the second derivative of the function depicts the change in the attenuation rate of LST, as shown in Fig. 6. From the urban core to the periphery, the attenuation rate of LST experiences an initial increase followed by a decrease. By examining the first derivative of the function, we can see three points denoted by p_1 , p_2 , and p_3 in Fig. 6 (coordinates r_1 , r_2 , and r_3 , respectively), which divide the attenuation of LST into four stages. From the center of the concentric rings to r_1 , the decrease rate of LST is slow, representing the hottest area of the city. From r_1 to r_2 , the decrease rate of LST rapidly increases to the maximum value, and LST still maintains a relatively high value, representing the sub-core of UHI (inner urban zone). The decreasing rate of LST gradually slows down from r_2 to r_3 , representing the fringe of UHI (urban-rural integration region). Finally, LST gradually stabilizes in the non UHI area, i.e., the periphery with fewer human activities. p_3 is the point where LST experienced a rapid decline and began to stabilize again, and f_{r_3} is the background temperature of rural areas (or surrounding non UHI areas). Since p_3 is the point where the first derivative changes the fastest, it needs to be solved with the second derivative of the inverse S-shaped function. The solution process is as follows:

The first derivative of Eq. (15) is:

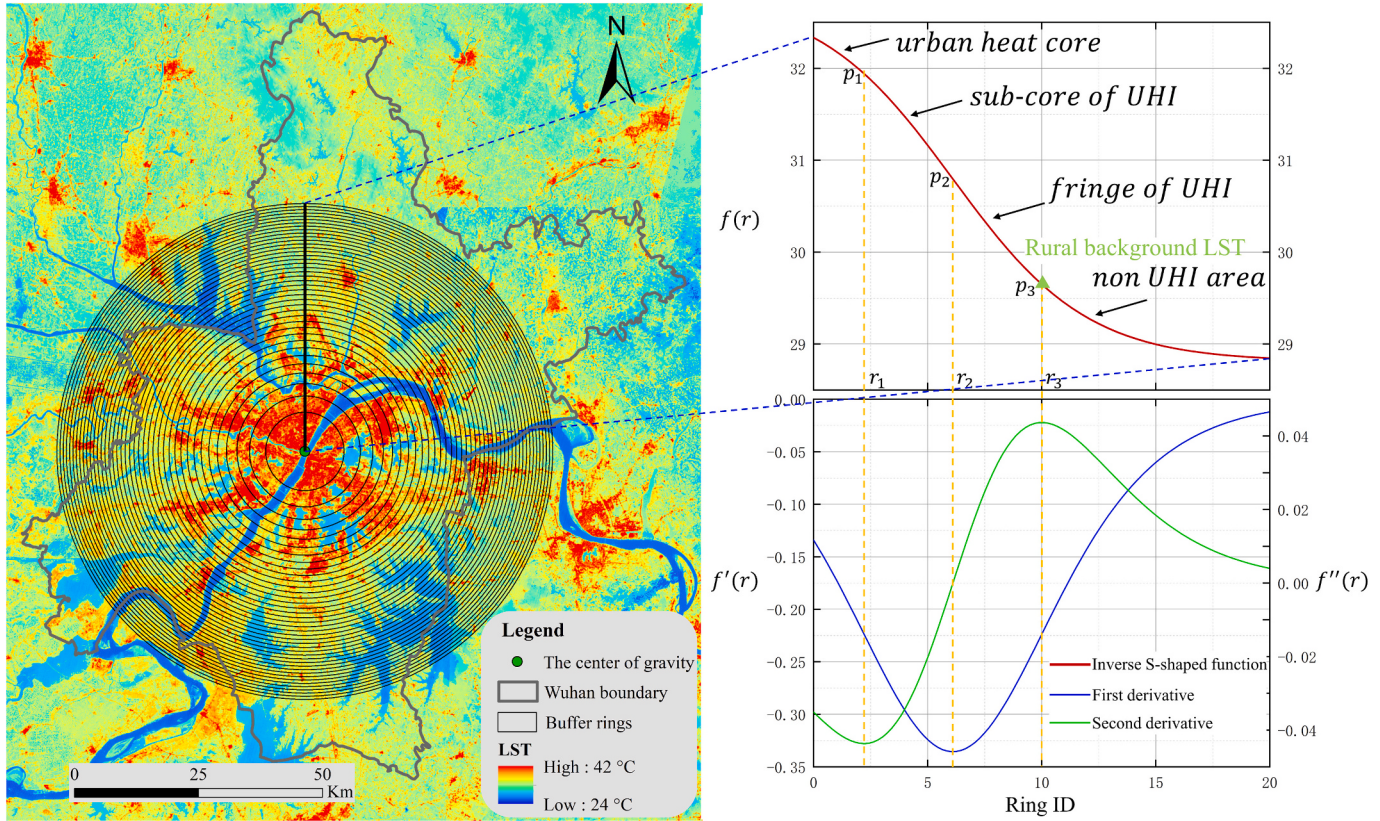


Fig. 6. Buffer rings, LST, and a schematic showing how rural background temperature is determined using the inverse S-shaped function.

$$f' = -\frac{2\alpha(t-c)}{D} \frac{e^{\alpha((2r/D)-1)}}{(1+e^{\alpha((2r/D)-1)})^2} \quad (16)$$

Eq. (15) can be transformed into:

$$1 - \frac{f-c}{t-c} = \frac{e^{\alpha((2r/D)-1)}}{1+e^{\alpha((2r/D)-1)}} \quad (17)$$

Then Eq. (16) can be rewritten as:

$$f' = -\frac{2\alpha(t-c)}{D} \frac{f-c}{t-c} \left(1 - \frac{f-c}{t-c}\right) \quad (18)$$

Let

$$h = \frac{f-c}{t-c} \quad (19)$$

Then

$$f' = -\frac{2\alpha(t-c)}{D} h(1-h) \quad (20)$$

Because $-\frac{2\alpha(t-c)}{D}$ is a negative constant, f' reaches its lowest negative value when $h = 0.5$, indicating the point (p_2 in Fig. 6) where the LST decreases most rapidly. The coordinates and the corresponding LST of p_2 can be calculated, i.e., $r_2 = D/2$, $f(r_2) = (t+c)/2$.

The second derivative of Eq. (15) is:

$$f'' = -\frac{2\alpha(t-c)}{D}(1-2h)h' = \frac{4\alpha^2(t-c)}{D^2}(2h^3 - 3h^2 + h) \quad (21)$$

Take the derivative of h in the second derivative:

$$\frac{df'}{dh} = -\frac{4\alpha^2(t-c)}{D^2}(6h^2 - 6h + 1) \quad (22)$$

We can obtain the two extreme points (denoted by p_1 and p_3 in Fig. 6) of the second derivative when $df'/dh = 0$, which $h = 1/2 \pm 1/\sqrt{12}$, i.e.,

$h_1 \approx 0.7887$ and $h_2 \approx 0.2113$. By Eqs. (17) and (19):

$$r = \frac{D}{2} \left(\ln \left(\frac{1-h}{h} \right) / \alpha + 1 \right), f = h(t-c) + c \quad (23)$$

Then the coordinates of p_1 and p_3 can be calculated as follows:

$$r_1 = \frac{D}{2} \left(\frac{-1.3171}{\alpha} + 1 \right), f_{r_1} = 0.7887(t-c) + c \quad (24)$$

$$r_3 = \frac{D}{2} \left(\frac{1.3171}{\alpha} + 1 \right), f_{r_3} = 0.2113(t-c) + c \quad (25)$$

where r_1 represents the scope of the urban heat core, and f_{r_1} can be described as the temperature at the edge of the urban heat core. Similarly, r_3 represents the scope affected by UHI and f_{r_3} represents the rural background temperature. Moreover, $r_1 + r_3 = D$, which denotes the sum of the extent of the urban heat core and the diameter affected by UHI. Thus, the comparison of parameter D in different periods can reflect the change in the extent of UHI effect.

3.1.4. SUHI intensity level calculation

SUHI intensity is calculated as the urban-rural average temperature difference (Schwarz et al., 2011):

$$\Delta T = T_{\text{Urban}} - T_{\text{Rural}} \quad (26)$$

where T_{Urban} is the average LST of the UMBA and T_{Rural} is that of the rural background temperature. Due to the LST difference of pixels, the impact of UHI on residents is also variant. The larger temperature difference means that the urgency of cooling in this area is higher. As shown in Table 1, the SUHI intensity level for a pixel (i,j) is defined and it's also convenient for the comparison of SUHI intensity for different periods.

Table 1
Definition of SUHI intensity levels.

SUHI intensity level	Definition
Level 1	$T_{Rural} \leq T_{ij} < T_{Rural} + \Delta T_{ij}$
Level 2	$T_{Rural} + \Delta T_{ij} \leq T_{ij} < T_{Rural} + 2\Delta T_{ij}$
Level 3	$T_{Rural} + 2\Delta T_{ij} \leq T_{ij} < T_{Rural} + 3\Delta T_{ij}$
Level 4	$T_{Rural} + 3\Delta T_{ij} \leq T_{ij} < T_{Rural} + 4\Delta T_{ij}$
Level 5	$T_{ij} \geq T_{Rural} + 4\Delta T_{ij}$

3.2. Modeling of SUHI cooling

3.2.1. General description of the proposed model

MACO is based on the traditional ant colony algorithm, which adds the competition and interaction mechanisms among different ant colonies to solve multiple land use allocation problems (Liu et al., 2012). The proposed thermal knowledge-informed MACO model follows the basic mechanism of the MACO model but endows artificial ants with thermal perception and evaluation capabilities. The flowchart of the proposed model is shown in Fig. 7. In MACO, the number of ant colonies is the same as the number of land use types, and the number of initial ants in each colony is determined by the number of pixels in each type. Initially, each pixel is randomly occupied by one ant, and the final locations of the ants are exported as an optimal land use layout scheme. Using the objective function, the ants can evaluate the current pixel and determine whether to occupy it. To realize the dynamic adjustment of land use type and quantity, we modified the search strategy of MACO. The search subject was set as the pixel instead of the ant, and each pixel determined the most appropriate land type by calculating the suitability

of each type of ant colony. In particular, the search space for each ant in the original MACO is the entire image, while the current search space for each pixel is K (number of land use types), improving the efficiency of the algorithm and adaptively changing the land use quantitative structure (Zhang et al., 2021). Accordingly, the exchange strategy is set as follows: if the objective function changes toward the expected target more than in the previous iteration, then the candidate ant takes over the pixel; otherwise, the pixel remains as the current type.

MACO simulates the natural behavior of ant colonies of using pheromone to find food. In the land use optimization problem in this study, each pixel has the pheromone intensity of K types of ant colonies (land use types). If the pixel is more suitable for a specific ant colony k , then that colony will gradually win in the competition and keep depositing pheromone. In the final stage, the probability of this pixel being occupied by ant colony k will be considerably greater than those of other types. As the most important step in optimizing the land type of pixels, the selection probability of pixel (i,j) by k -type ant at iteration t $P_{ijk}(t)$ can be defined as follows:

$$P_{ijk}(t) = \frac{[\tau_{ijk}(t)]^\alpha [\eta_{ijk}(t)]^\beta}{\sum_{type \in K} [\tau_{ijtype}(t)]^\alpha [\eta_{ijtype}(t)]^\beta} \quad (27)$$

where $P_{ijk}(t)$ is determined by two factors: $\eta_{ijk}(t)$, the heuristic value of ant colony (land use) k at pixel (i,j) , and $\tau_{ijk}(t)$, the pheromone intensity of ant colony (land use) k at pixel (i,j) . The heuristic value is introduced as prior knowledge to guide the initial search of ant colonies and pheromone intensity is the basis of the positive feedback mechanism of MACO. Constants α and β are used to adjust the relative importance of

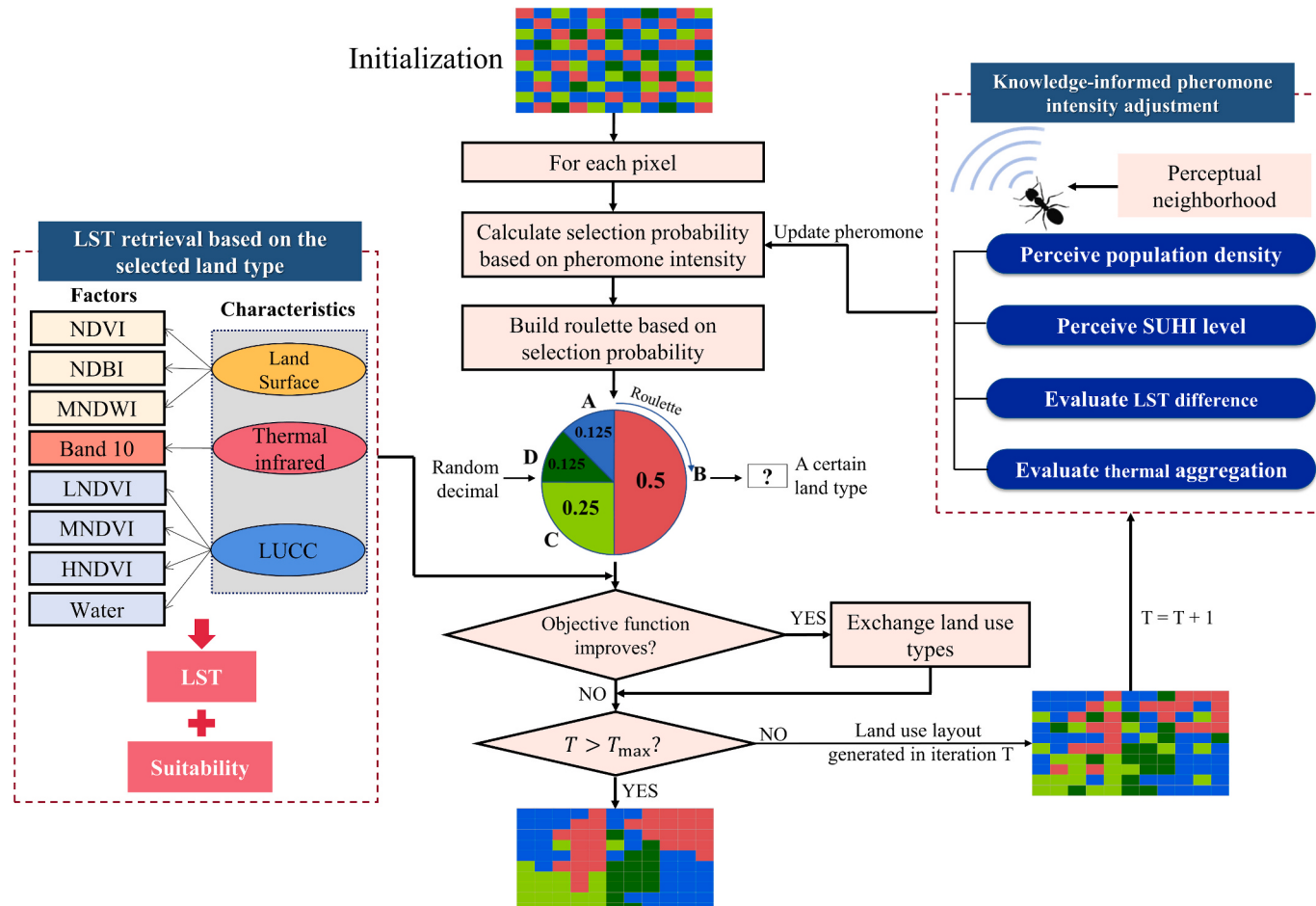


Fig. 7. Flowchart of thermal knowledge-informed MACO model.

the two factors, which were assigned as 0.75 and 1.25 in this study, respectively (Liu et al., 2012).

The heuristic value can improve search efficiency by providing different privileges to certain land use types of each pixel, which can be measured by land use suitability:

$$\eta_{ijk} = \frac{\text{Suit}_{ijk}}{\sum_x \text{Suit}_{xk}} \quad (28)$$

where η_{ijk} represents the heuristic value of ant colony k at pixel (i, j) ; Suit_{ijk} represents the suitability of land use k at pixel (i, j) ; $\sum_x \text{Suit}_{xk}$ represents the sum of the suitability of land use k in the whole study area.

Pheromone intensity $\tau_{ijk}(t)$ is the unique factor that guides the algorithm in realizing land use optimization, which is initialized as:

$$\tau_{ijk}(t=0) = \frac{1}{G} \quad (29)$$

where G is the total number of pixels in the whole study area. Pheromone intensity is updated at each iteration through two processes: (1) enhancing the pheromone intensity of the current ant colony at the end of each iteration if the type of the pixel is changed, and (2) decreasing the pheromone intensity of other ant colonies (i.e., evaporation), in which the updating process is defined as:

$$\tau_{ijk}(t+1) = \tau_{ijk}(t)(1 - \rho) + \Delta\tau_{ijk}(t) \quad (30)$$

$$\Delta\tau_{ijk}(t) = \begin{cases} r \cdot \tau_{ijk}(0) = \frac{r}{G} & \text{if the type of pixel } (i, j) \text{ is changed to } k \\ 0 & \text{others} \end{cases} \quad (31)$$

where ρ is a coefficient that controls the evaporation rate of the pheromone to prevent the algorithm from converging too quickly to the locally optimal land use type, and it is set to 0.01 in this study; $\Delta\tau_{ijk}(t)$ refers to the pheromone left by the k -type ant at pixel (i, j) , which is determined by the initialized $\tau_{ijk}(0)$; and r is a coefficient for adjusting the added value of the pheromone. After multiple iterations, the pheromones of the specific ant colony on different pixels will occupy the dominant position according to the pheromone updating, and thus, stable and optimal land use allocation can be outputted during the final stage.

3.2.2. Objective function

Two objectives of land use optimization were determined. The first objective was to maximize land suitability. In the context of remote sensing image processing, maximizing land suitability also implies minimizing the difference between the optimized and original land types to maintain consistency with the original land layout. The second objective was to minimize the difference between current LST and the set cooling reference temperature, which attempted to cool the high-temperature area. To balance the numerical differences and avoid potential conflicts between the two objectives, we normalized both objectives and employed the weighting method as follows:

$$F_{ij} = \max_k (\mu^* \text{Suit}_{ijk} - \nu^* \text{abs}(LST_{ijht} - LST_{ijk})) \quad (32)$$

where μ and ν are the weights of land suitability and LST cooling, respectively, and $\mu = \nu = 0.5$ considering that land suitability and LST cooling are equally important in this study; Suit_{ijk} refers to the suitability of pixel (i, j) for land use type k ; LST_{ijk} is the LST of the optimized land use type k ; and LST_{ijht} denotes the cooling reference value for approximating the human body comfort temperature. Human body comfort temperature is influenced by factors such as relative humidity and air flow, and thus, quantifying it with a specific value is difficult. In this study, LST_{ijht} intends to set a cooling reference to adjust the temperature as appropriately as possible. In accordance with to existing research, the value

was set to 26 °C (Liu et al., 2022; Zhang et al., 2021).

3.2.3. Suitability

In Section 3.1.2, we divided the study area into four land use types and established their functional relationships with LST. Considering that changing a water body is difficult, we set the optimization objective to the three other types of land use. Referring to Zhang et al. (2021), we used the quantitative remote sensing index to measure the suitability of different land use types, i.e., the difficulty in changing the current land use type. In particular, the NDVI was used to measure the suitability of the HNDVI (e.g., forest land) land, and the normalized difference built-up index (NDBI) was used to measure the suitability of the LNDWI (e.g., impermeable surface), for which NDBI is calculated as follows:

$$NDBI = \frac{R_{MIR} - R_{NIR}}{R_{MIR} + R_{NIR}} \quad (33)$$

where R_{NIR} and R_{MIR} refer to the reflectance of the near-infrared and mid-infrared bands. With regard to the MNDVI (e.g., grassland), we set the NDVI value of 0.6 as the most suitable value, because it is inappropriate to convert to MNDVI when NDVI is excessively high or low. After normalization, all the pixels gained the suitability of the three land use types with a value of 0–1.

In addition, the values of the thermal infrared band (i.e., band 10) and land surface emissivity should be updated after the land use type changes because these two factors are essential for LST retrieval (Chen and Zhang, 2017; Yu et al., 2014). Considering that the land surface emissivity of different land types is only related to NDVI, this study designed two strategies for updating the value of the thermal infrared band and NDVI after land use type was modified. (1) The lowest value of the thermal infrared band and the highest value of NDVI that correspond to the candidate land type in the original image are used. This strategy intends to obtain the maximum cooling potential, and it is used in the algorithm iteration. (2) A buffer zone is set up with the optimized pixel as the center. The average values of the thermal infrared band and NDVI that correspond to the candidate land type in the buffer zone are used. This strategy intends to simulate the actual cooling effect by considering regional heterogeneity, and it is used for the final result output.

3.2.4. Pheromone intensity updating based on thermal environment perception

In the current evaluation and exchange framework of the MACO algorithm, ants can only evaluate the suitability and LST of their pixels and cannot perceive the surrounding environment. In addition, ants cannot obtain urban information, such as the degree of population aggregation and SUHI intensity levels. In this study, artificial ants were transformed using two methods:

- (1) Enhance the self-perception ability of ants. BUD and SUHI intensity level data were used to expand the perception information domain of ants. The cooling requirement was determined by evaluating whether the pixel was located in a densely populated area. In particular, low population density areas (e.g., rural and industrial parks) remain unchanged, while densely populated areas exhibit a high demand for cooling. At this moment, the pheromone intensity of impervious surfaces can be reduced, promoting land use transition, which can be expressed as:

$$\tau_{ijis}(t) = \begin{cases} \tau_{ijis}(t) & \text{if } pop_{ij} \leq pop_{mean} \\ \tau_{ijis}(t) * \left(1 - \frac{pop_{ij} - pop_{mean}}{pop_{max} - pop_{mean}}\right) & \text{others} \end{cases} \quad (34)$$

where pop_{ij} is the BUD of pixel (i, j) ; pop_{mean} is the mean BUD of the study area; and pop_{max} is the maximum value of BUD. In addition, the ants are endowed with the ability to recognize SUHI intensity levels. The pheromone intensity of the current land type of pixel (i, j) will be reduced if

the SUHI intensity level is high, which can be expressed as:

$$\tau_{ijk}(t) = \begin{cases} \tau_{ijk}(t) & \text{if SUHI intensity level} < 3 \\ \tau_{ijk}(t)^*\theta_l & \text{others} \end{cases} \quad (35)$$

where the pheromone intensity attenuation coefficients θ_l of SUHI intensity levels 3, 4, and 5 were set to 0.9, 0.8, and 0.7, respectively.

- (2) Add the surrounding-perception ability of ants. Some areas in the city may exhibit excessive temperature differences from their surrounding areas due to human activities and unreasonable land allocation. Therefore, in the iteration of the optimization algorithm, ants should consider the temperature difference between themselves and their surrounding environment to evaluate whether the pixel (i, j) is located in an abnormally high-temperature area. By constructing a perceptual neighborhood U for each ant, the optimization of the abnormal temperature zone can be expressed as follows:

$$\tau_{ijk}(t) = \begin{cases} \tau_{ijk}(t) & \text{if } DIFLST_{ij} > DIFLST_{abnormal} \\ \tau_{ijk}(t)^*\theta_z & \text{others} \end{cases} \quad (36)$$

$$DIFLST_{ij} = LST_{ij} - LST_{U_{ijp}} \quad (37)$$

$$\theta_z = 1 - \frac{DIFLST_{ij} - DIFLST_{abnormal}}{DIFLST_{max} - DIFLST_{abnormal}} \quad (38)$$

where θ_z is the pheromone intensity attenuation coefficients for controlling temperature difference; U_{ijp} is the perceptual neighborhood centered on ants at pixel (i, j) with a range of $p \times p$, and $LST_{U_{ijp}}$ is the mean LST of the perceptual neighborhood; $DIFLST_{ij}$ is the temperature difference of pixel (i, j) ; $DIFLST_{abnormal}$ and $DIFLST_{max}$ are constants, which represent the values of abnormal and maximum temperature differences, respectively. With urban construction, some areas where high-level SUHI intensity has accumulated gradually become heat cores.

This may lead to thermal injury events owing to the inadequacy of cooling facilities in these regions (Hu et al., 2019). Therefore, artificial ants should evaluate the aggregation of high-level SUHI intensity in their perceptual neighborhood to disintegrate the heat core area by optimizing land use type, which the process can be expressed as:

$$\tau_{ijk}(t) = \begin{cases} \tau_{ijk}(t) & \text{if } \sum_{x,y \in U_{ijp}} HI_{xy} < \sum_{i,j \in N, x,y \in U_{ijp}} HI_{xy}/n \\ \tau_{ijk}(t)^*\theta_c & \text{others} \end{cases} \quad (39)$$

where HI_{xy} is the value of high-level SUHI intensity (i.e., levels 4, and 5) at pixel (x, y) , which is located in the perceptual neighborhood of pixel (i, j) ; N is the whole image, and n is the number of pixels with three types of land use to be optimized; θ_c is used to reduce the pheromone intensity of the current land use type in the heat core, and the larger the value, the higher the probability that the current land use type will be changed, which is set to 0.8 in this study.

4. Results and analysis

4.1. Characteristics of SUHI

4.1.1. SUHI influencing scope measured by UMBA boundary

As shown in Fig. 8a, the regions with higher BCI values are distributed on both banks of the Yangtze River in the central region, while the BCI values in non-urban areas are generally less than -0.1. Therefore, the impermeable surface of Wuhan was extracted based on the threshold value of BCI. Meanwhile, we randomly generated 100 sample test points to validate the extraction accuracy. By comparing them with the high-precision remote sensing image of Google Maps, the extraction consistency of impermeable surfaces was 91%. The spatial distribution of the impervious surface was characterized by dense in the center and sparse in the periphery as shown in Fig. 8b. To characterize the gradual outward diffusion of the impervious surface and quantify its density, the

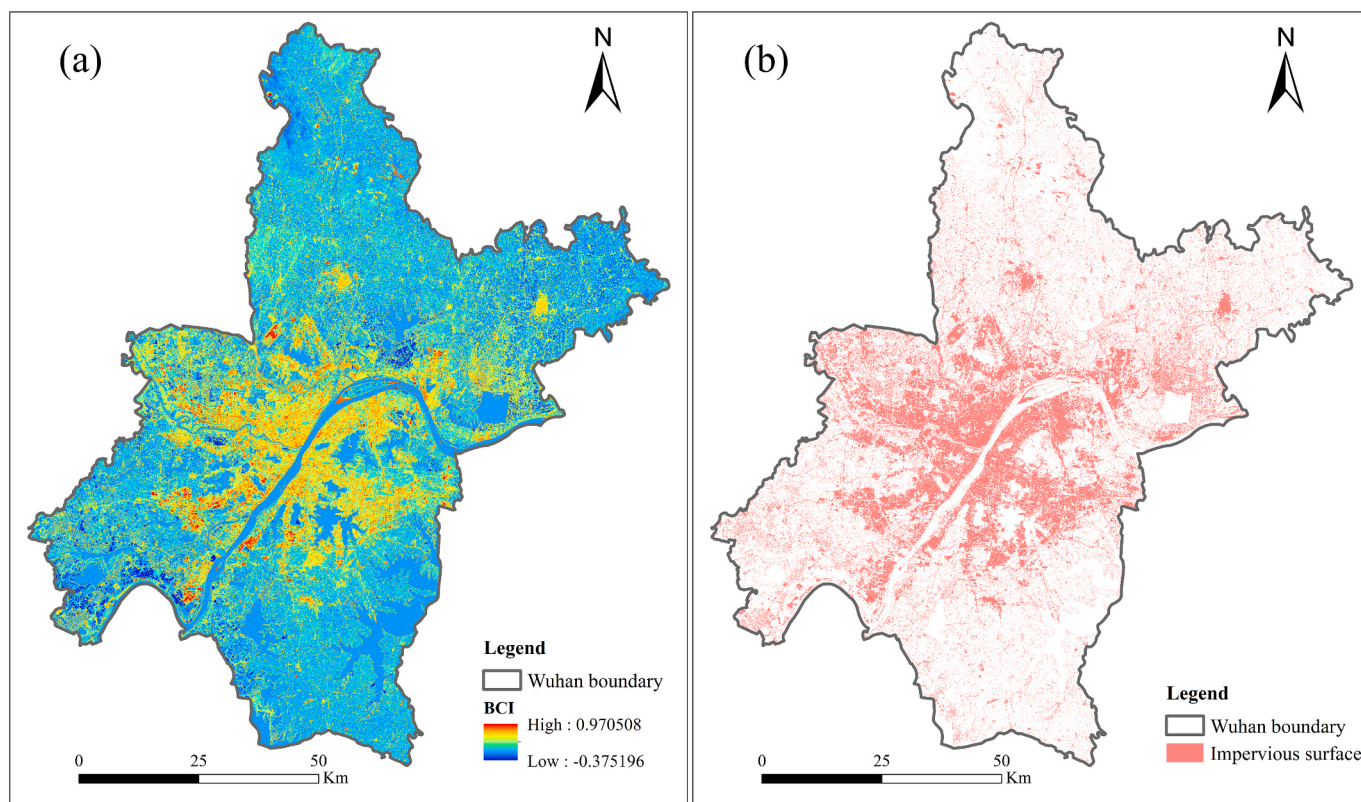


Fig. 8. Spatial distribution of (a) BCI and (b) impervious surface.

ISDD was calculated. The neighborhood range r of the central pixel will affect the calculation result of ISDD. When r is 1500 m, the ISDD patch exhibited continuity and presented the distribution characteristics of Wuhan large-scale impervious surfaces, which was used in this study.

Fig. 9a shows the spatial distribution of different impervious surface densities, where the high-density areas ($\text{ISDD} > 70\%$) are concentrated in the commercial center with the densest buildings in Wuhan, and the edge of the low-density areas (ISDD is within 35–50%) is similar to the planning boundary of Wuhan Urban Development Zone. Take ISDD with $>35\%$, $>50\%$, and $> 70\%$ pixel distribution as input data of CCA with parameters $L = 200$ m and patch threshold $S = 10,000$, **Fig. 9b** shows the result of UMBA boundary extraction. Using the same method, we also extracted the UMBA boundary of Wuhan in 2016 (**Fig. 9c**). It can be seen that Wuhan's UMBA has experienced rapid expansion, and the scale of medium-high density areas has increased significantly. As the most concentrated area of human activities, the extraction of the UMBA boundary can help us determine the impact scope of UHI, and it is also the main focus area of heat island cooling (Meng et al., 2018).

4.1.2. SUHI intensity based on urban-rural LST difference

Considering that Wuhan is a polycentric city with three urban centers close to each other, we chose the center of the triangle formed by the three centers to construct the concentric rings. We calculated the average value of LST in each concentric ring and used the nonlinear least squares method in MATLAB R2021a. The fitting curve of the urban-rural LST decrease for 2016 and 2022 is shown in **Fig. 10**. The adjusted R^2 of 2016 and 2022 is 0.97 and 0.98, respectively, indicating that the inverse S-shaped function can fit the distance decay of LST well. Spatially, the LST decreased with the distance from the urban center, where LST first decreased slowly, then dropped down quickly, and finally decreased slowly again. Moreover, when LST decreased in 2016, the slope of the curve increased, indicating a relatively clear spatial boundary between the urban and rural areas (**Fig. 10a**). The decline rate of LST in 2022 was significantly slower, indicating that with the development and construction of cities, the urban-rural boundaries of China's major cities are becoming blurred, and cities and rural areas are gradually moving toward integration (**Fig. 10b**). The results also prove that delineating the boundaries between the cities and rural areas of metropolises is inappropriate. In addition, remote sensing data from different seasons from 2016 to 2022 were used for testing, and the fitting R^2 values for all seasons are relatively high (>0.95) except for winter. The influence range of the heat island in summer is smaller than that in spring and fall and the lower the temperature in the same year, the greater the range of

heat island impact according to the changes in parameters t and c , which is consistent with the existing conclusions (Meng et al., 2018). The fitted parameters (α , D , r_1 , and r_3) show similar trends in different years within the same season, which proves the robustness of the inverse S-shaped function in comparative analysis of long time series in the same season (see Supplementary Fig. S3 and Table S1). In winter, however, due to the small temperature difference between urban and rural areas in Wuhan, the fitting R^2 of the inverse S-shaped function is relatively low, making it difficult to capture the significant UHI effect, which is similar to previous research findings (Huang et al., 2019; Sun et al., 2019).

The parameters of the function are shown in **Table 2**, which reflects the temporal variations in urban-rural LST characteristics. Parameters t and c represents the background LST in the urban heat core and hinterland, respectively. The two parameters increased markedly from 28.81 °C and 32.78 °C in 2016 to 30.04 °C and 33.18 °C in 2022. Although LST varies across years, considering that the hottest days in August were selected for 2016 and 2022, the increase in temperature of urban core and hinterland indicates that the challenge of high temperatures to urban sustainable development is becoming increasingly severe. Parameter r_1 and r_3 characterize the range of urban heat core and the diameter affected by UHI. With the expansion of the urban impervious surface, the values of the two parameters have significantly increased, especially the range of urban heat core. Correspondingly, the value of D also increased. Combining parameters α and D in Eq. (25), the rural background temperature values for 2016 and 2022 were determined as 29.74 °C and 30.70 °C, respectively. Additionally, based on the urban average temperature within the boundary of UMBA (31.15 °C in 2016 and 32.85 °C in 2022), the SUHI intensities for 2016 and 2022 were calculated using Eq. (26), which are 1.61 °C and 2.15 °C, respectively.

SUHI intensity avoids a direct comparison of specific temperatures across years and intuitively displays the LST difference between urban and rural areas. Furthermore, SUHI intensity was divided into several levels. Due to the UHI effect mainly affecting urban areas, the following analysis will be carried out based on urban development zones. As shown in **Fig. 11**, SUHI intensity was mainly at a low level, and high-level SUHI intensity mainly existed in industrial parks outside the Third Ring Road, such as the Dongfeng Automobile New Energy Plant, Wuhan Iron and Steel Industrial Park, etc. We compared SUHI intensity levels in 2016 and 2022: the UHI impact range significantly expanded, indicating the rapid expansion of the city. In 2022, the number of high-level SUHI intensity pixels (i.e., levels 4 and 5) was less than that in 2016, and there were few extremely strong SUHI intensities in the main

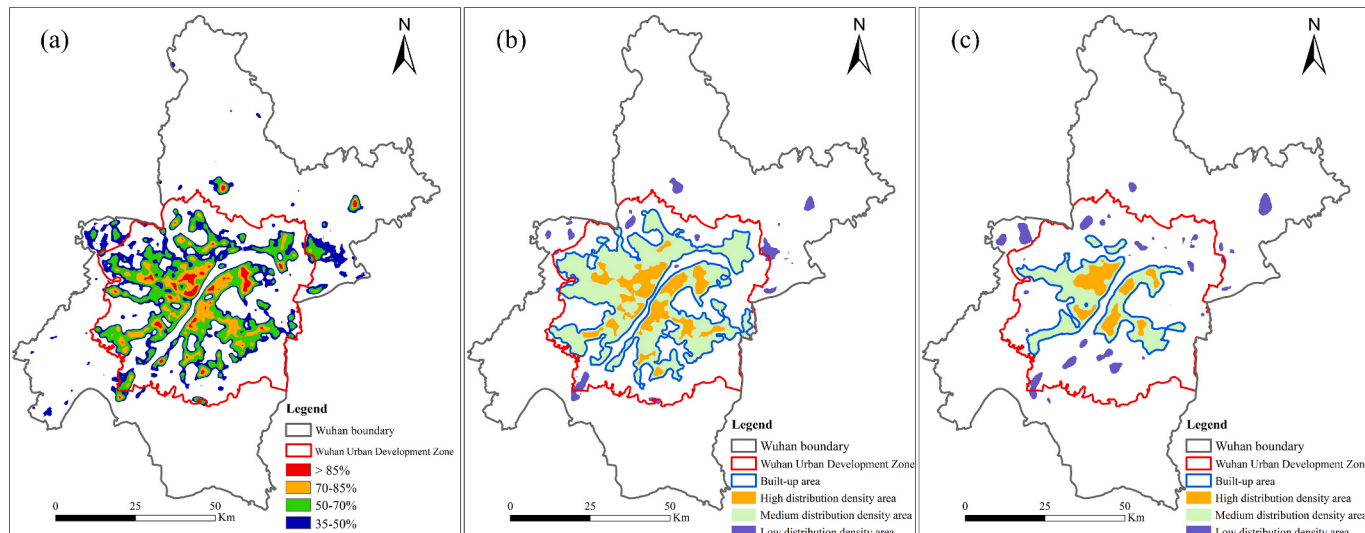


Fig. 9. Spatial distribution of (a) impervious surface density, (b) UMBA boundary in 2022, and (c) UMBA boundary in 2016.

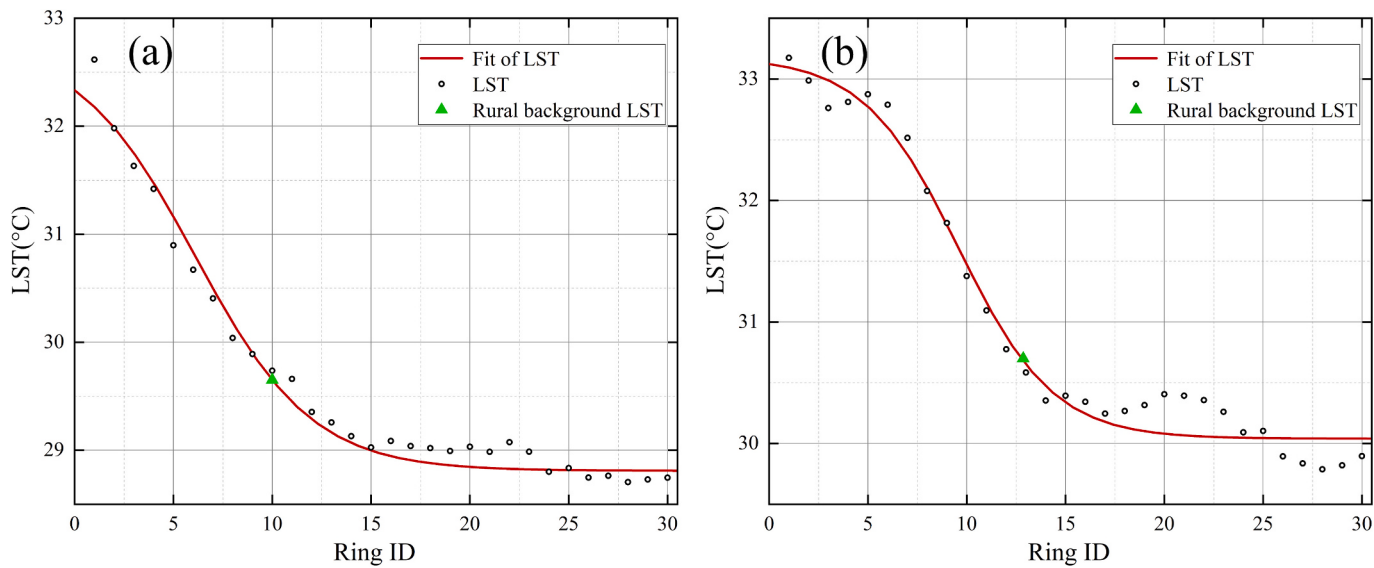


Fig. 10. Fittings of LST in (a) 2016 and (b) 2022.

Table 2
Parameters of the urban-rural LST decreasing functions.

City	Year	α	D	t	c	r_1	r_3
Wuhan	2016	2.066	12.22	32.78	28.81	2.21	10.01
	2022	3.99	19.16	33.18	30.04	6.42	12.74

urban areas of Wuhan, indicating that the construction of urban parks and green spaces effectively improved the livability of the urban thermal environment. The gradual relocation of logistics warehousing and industrial parks has also alleviated the intensification of the UHI effect in the main urban areas (Wang et al., 2022a).

4.2. Cooling of SUHI

4.2.1. Model implementation and comparison analysis

The algorithm iteration termination condition was set to 99% similarity to the original image within 20 iterations and 10 independent runs were repeated for each optimization experiment. Notably, the model is not committed to reducing the average LST of UBMA significantly because the number of pixels that can be modified is extremely limited under the constraint of similarity. Increasing the area of green space on a large scale can effectively reduce LST, but the huge cost of greening is difficult for local governments to accept. Therefore, the model focuses on areas that urgently require cooling rather than on changing land use types at a large scale throughout the entire research area. This is

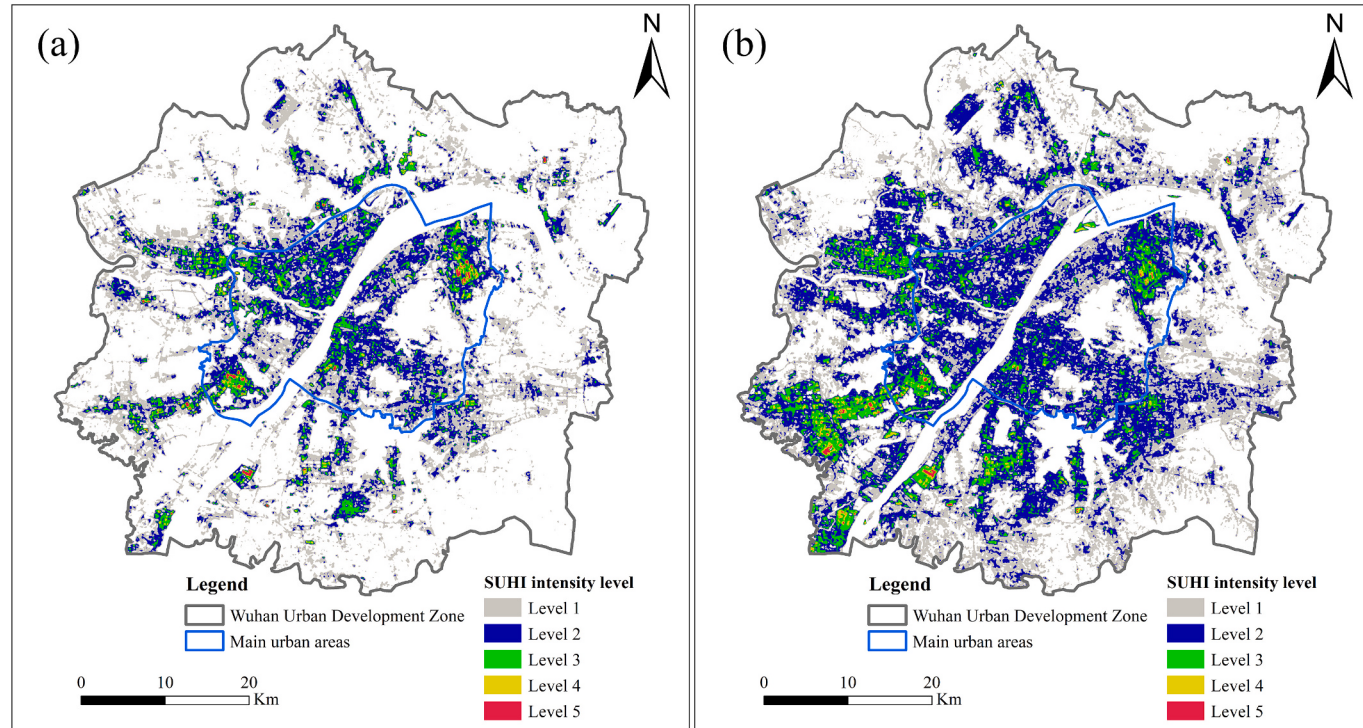


Fig. 11. Spatial distribution of SUHI intensity level in (a) 2016 and (b) 2022.

consistent with the greening planning of cities with limited budgets (Chen et al., 2022). As shown in Fig. 12, the initially randomly distributed land use types gradually became similar to the original image and remained stable through a small number of iterations. In addition, under a similarity setting of 90% to 98%, the spatial position of the optimized pixels is shown in Fig. 13. As overall similarity increased, the optimized pixels gradually focused on high-level SUHI areas and eventually fixated on specific locations, especially when the similarity is >97%. When the optimized pixels are gathered in specific areas, the value of similarity is

more of a reflection of the cooling urgency, which depends on the local government greening budget. The optimized pixels have a higher priority for cooling down when the similarity is set to 99%, and the resulting financial expenditure pressure is acceptable. Table 3 indicates that land use conversion and modified types are mostly LNDVI and MNDVI, where the number of LNDVI decreased by 1.7% and the number of MNDVI increased by 1.5%. This finding indicates that the model tends to mitigate urban heat by adjusting the impermeable surface to the natural surface, instead of increasing the amount of urban forest land.

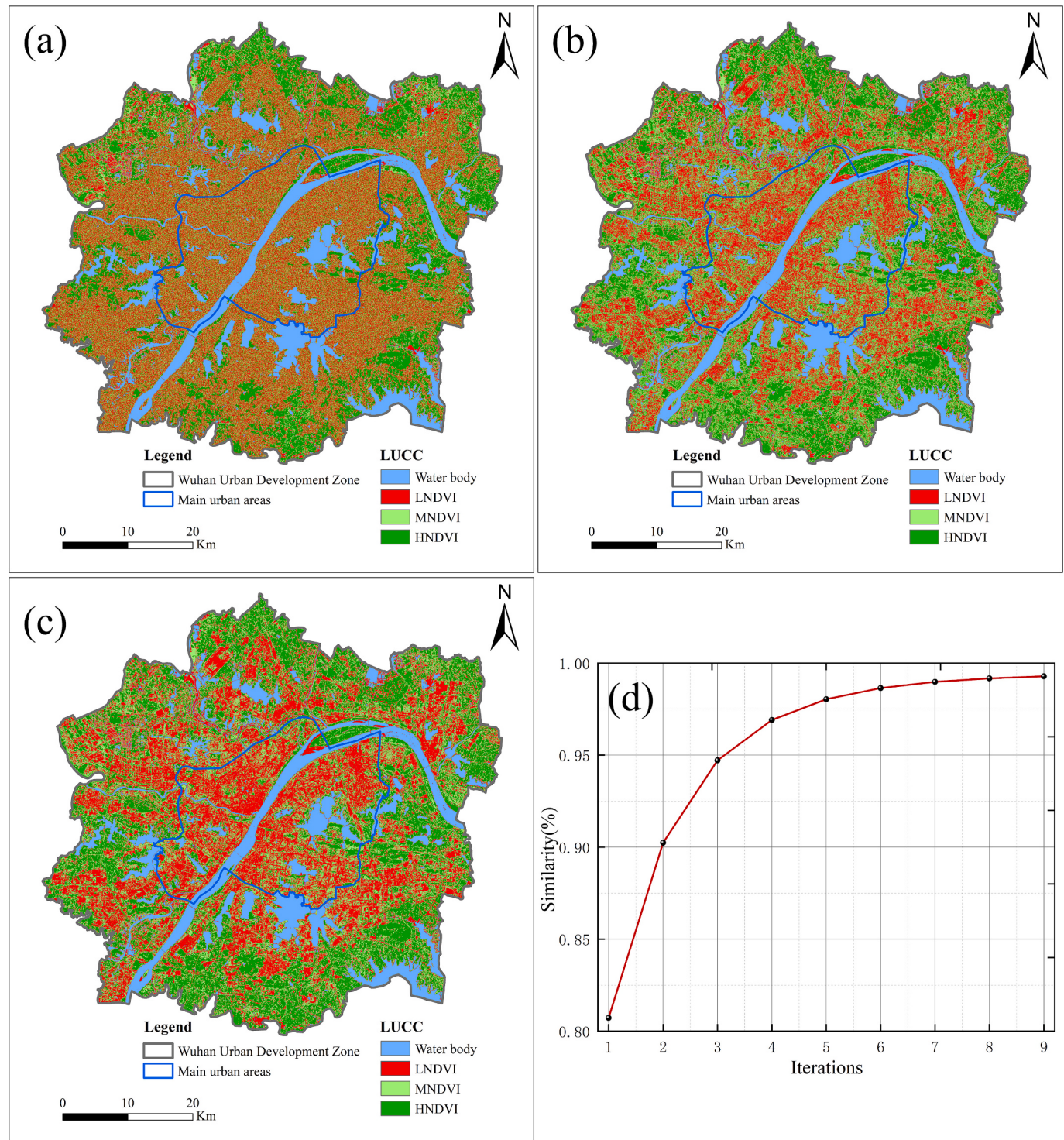


Fig. 12. Land use maps associated with iterations: (a) random initialization of pixels, (b) result of the first iteration, (c) final result of 9th iteration and (d) iterative similarity curves.

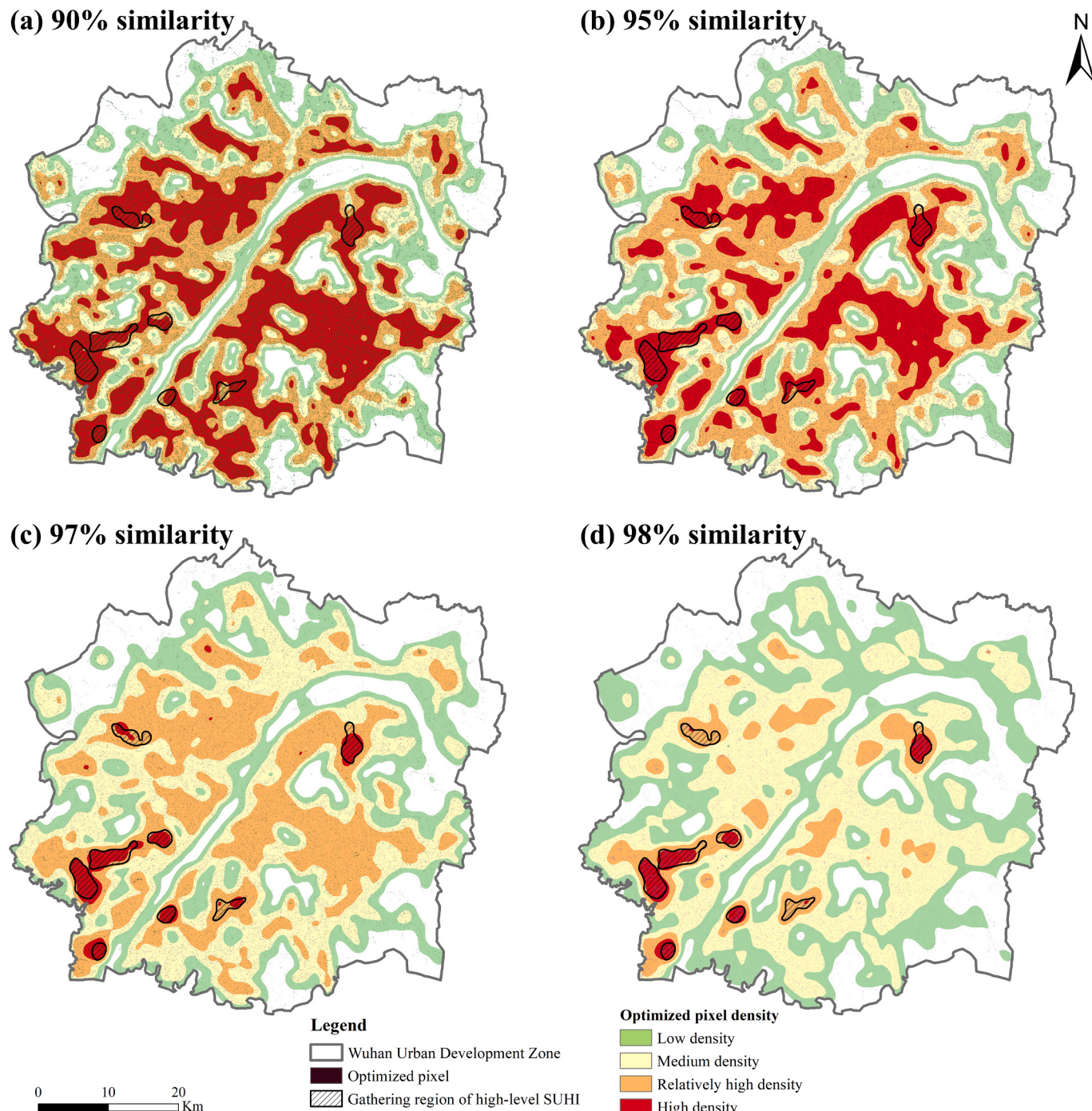


Fig. 13. Spatial distribution of the optimized pixels under different similarity settings.

Table 3
Land-use transfer matrix before and after optimization.

Original status	Optimal solution				Original total count
	Water	LNDVI	MNDVI	HNDVI	
Water	491,801	0	0	0	491,801
LNDVI	0	1,152,545	16,828	3792	1,173,165
MNDVI	0	1084	984,458	1861	987,403
HNDVI	0	0	1393	984,220	985,613
Optimal total count	491,801	1,153,629	1,002,679	989,873	–

This is reasonable because the difference between the LST of LNDVI and the cooling reference is significant. However, directly modifying it to HNDVI will result in a considerable loss of suitability. A small number of pixels were modified from MNDVI to LNDVI, and approximately 0.2% of HNDVI was modified to MNDVI. A possible explanation could be that the LST of these areas was lower than the set optimal temperature; therefore, the pixels were modified to reduce temperature difference.

To verify the improvements in the proposed model further, we conducted a comparative analysis with the traditional MACO model. After iterating 9 and 7 times respectively, the two models achieved nearly the same effect in reducing the average temperature of UBMA after modifying a similar number of pixels; however, a significant difference was observed in the cooling SUHI. In previous research, MACO

adopts a modified search and exchange strategy for maintaining spatial similarity with the original image and reducing LST (Zhang et al., 2021); however, it does not incorporate thermal-related knowledge. For example, MACO only considers the synergistic optimization of suitability and cooling but disregards the urgency of regional heat mitigation. Some areas with high-level SUHI are more prone to thermal injury events; however, MACO cannot give attention to these areas because optimization can lead to a significant reduction in land suitability (i.e., the cost of land conversion is heavy). This condition also leads to a more dispersed spatial distribution of pixels optimized by MACO (Fig. 14). By contrast, knowledge-informed MACO achieved a better SUHI cooling effect, decreasing the number of SUHI at levels 4 and 5 by 7.2% and 5.1%, respectively, and reducing the risk of residents being exposed to high-level SUHI (Table 4). Regarding the spatial distribution shown in Fig. 14, the constructed thermal-related knowledge encourages algorithms to search for suitable pixels in areas with high-level SUHI for optimization.

As shown in Fig. 12d, the matching degree of the map increased rapidly and gradually stabilized. With an initial similarity of approximately 0.58, the model exhibited high consistency with the original image after 7–9 iterations. The initial land use type of a large number of pixels was different from the original state due to the completely random initialization. As mentioned in Section 3.2.3, given that the model used the lowest value of the thermal infrared band and the maximum NDVI when calculating the LST of the pixel with modified land use type, the average temperature of the study area would be at the lowest level during the entire optimization after random initialization. As iteration proceeded, the objective function of improving land suitability led to a rapid increase in the matching degree of land use types. Therefore, when the land use map changed toward the original image, the average temperature of the study area exhibited a warming trend (Fig. 15). Eventually, the model reached a relatively stable state when the pixels modified for land suitability and temperature optimization reached relative equilibrium. In addition, the similarity of the MACO model increased faster, but the cooling effect for high-level SUHI was limited. No tendency or preference for pixel modifications was observed in the

Table 4
Cooling effects of the two models.

	Number of iterations	Number of modified pixels	Number of level-4 SUHI	Number of level-5 SUHI	Number of people exposed to high-level SUHI
Original status	–	–	26,498	3783	997,039
Knowledge-informed MACO	9	26,066	24,593	3590	943,581
MACO	7	26,735	26,302	3759	995,106

MACO model, and the number of high-level SUHI exhibited monotonic changes. For the knowledge-informed MACO model, the number of high-level SUHI fluctuated in the last few iterations, indicating that the model not only modified pixels for map matching but also considered the SUHI level and residents with a high risk of heat injury (Fig. 15).

4.2.2. Model effectiveness and policy implications

The optimized distribution of SUHI levels using the knowledge-informed MACO is shown in Fig. 16. The strategy of the local average value of thermal radiation and NDVI was not adopted during optimization because the thermal radiation values presented by various land use types in the local area were extremely close due to the flow of air and thermal diffusion of the underlying surface (Li et al., 2022b). The algorithm cannot effectively distinguish the cooling effect and suitability loss caused by land-type conversion, and thus, is unable to converge quickly. Given differences in multi-dimensional features such as surface characteristics, LST, population density, and surrounding thermal environment, spatial distribution of the modified pixels varies across the study area. Owing to the concentration of high-level SUHI in logistics warehousing land and industrial parks, most pixels modified by the model also appeared in these areas. Three local areas, namely, A, B, and C were selected to analyze the effectiveness of the model. Region A is located in the cookware production industrial park, where LST is

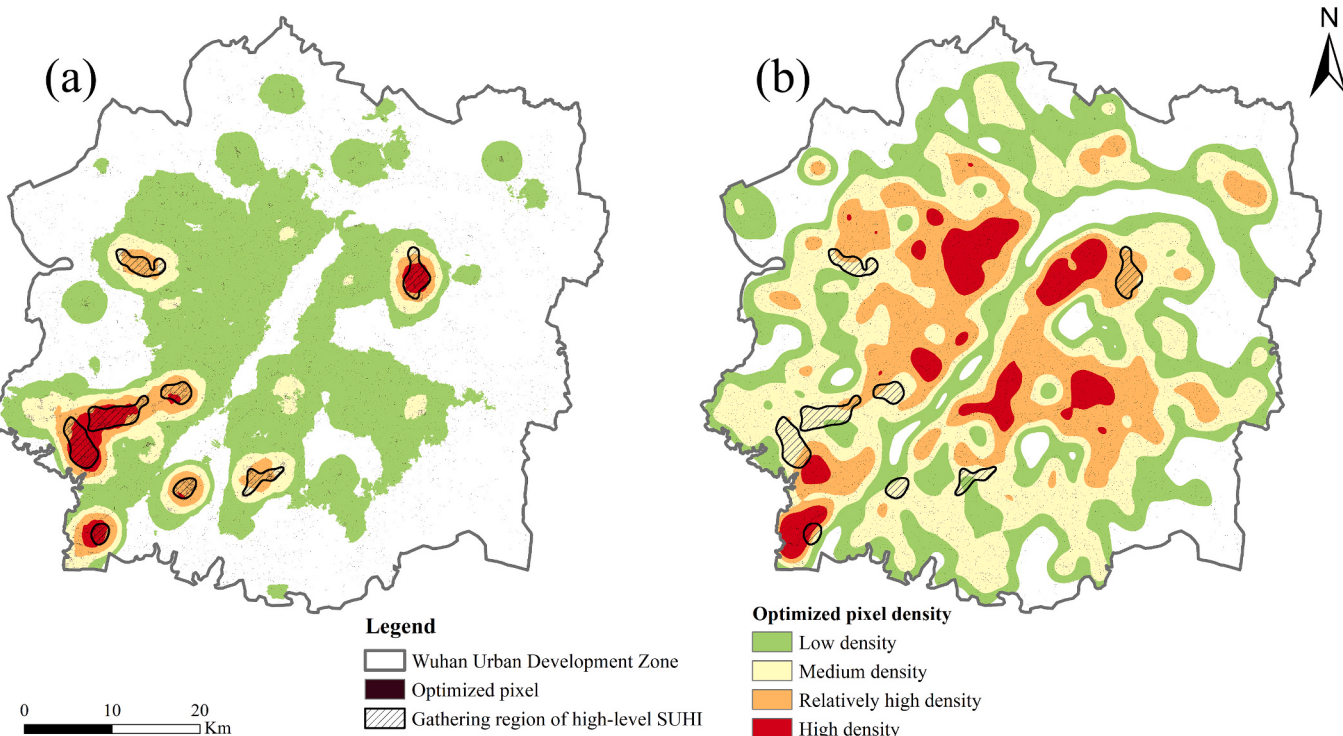


Fig. 14. Spatial distribution of the optimized pixels: (a) knowledge-informed MACO and (b) MACO.

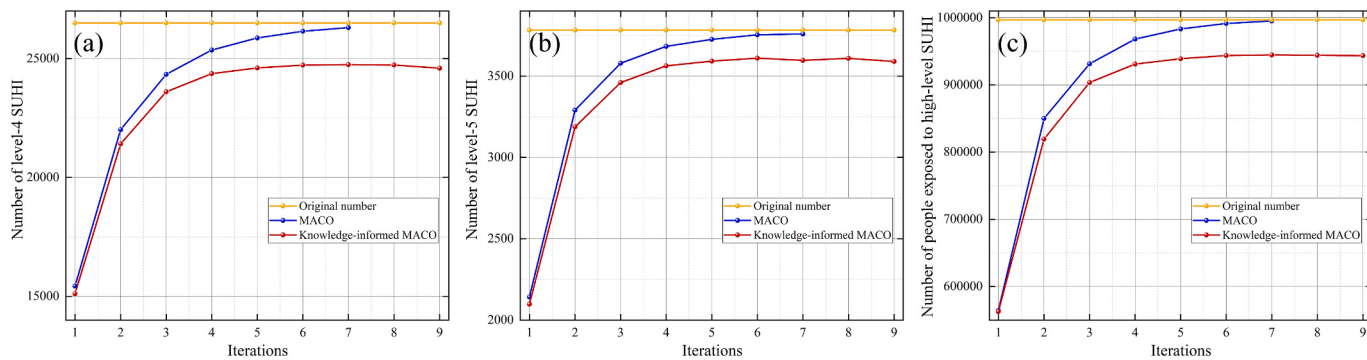


Fig. 15. Cooling effects vary with the number of iterations: (a) number of level-4 SUHI, (b) number of level-5 SUHI, and (c) number of people exposed to high-level SUHI.

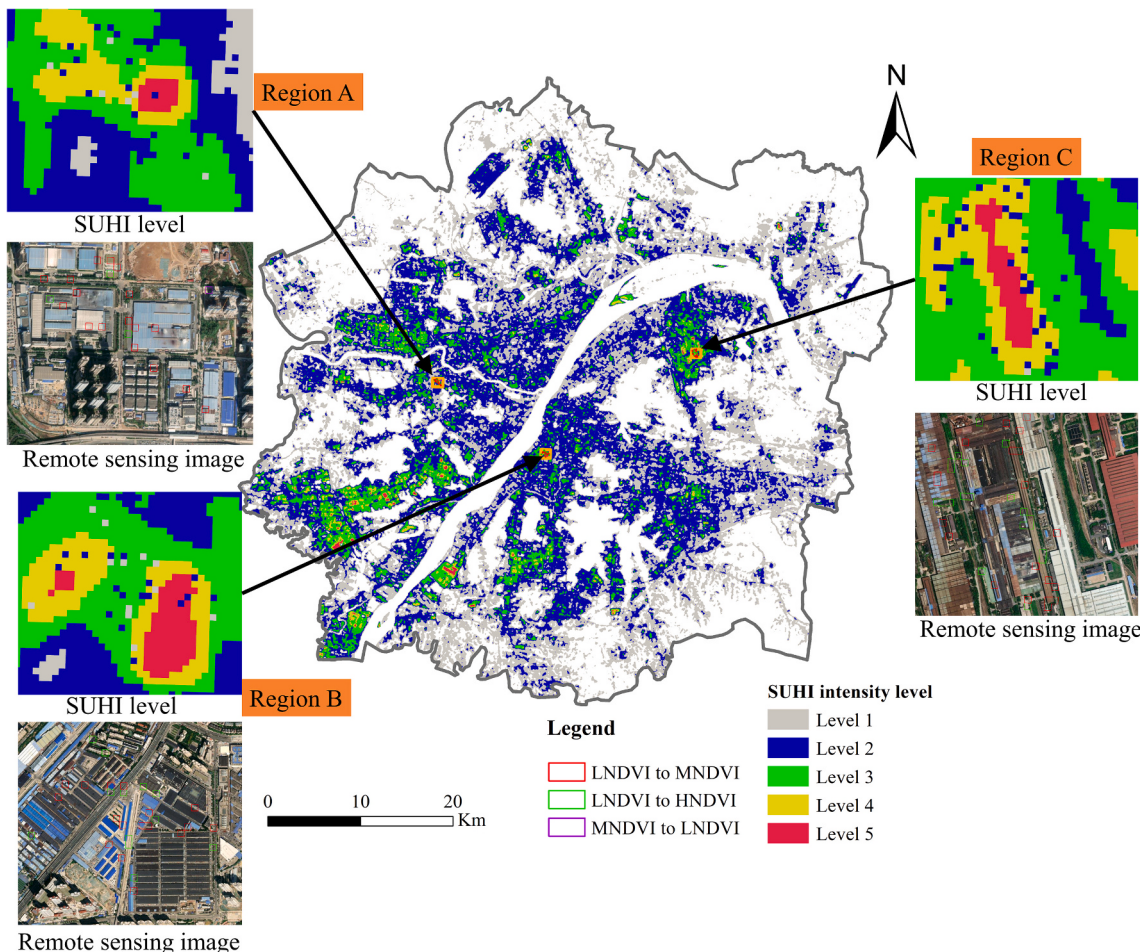


Fig. 16. Optimal effectiveness analysis.

significantly higher than that of the surrounding area, and four and five levels of SUHI exist. The reason for the abnormally high temperature in Region A can be the lack of cooling facilities and green surfaces, which deviates from the plan of “seeing green within 500m” of Wuhan City (Xing et al., 2020). The model captured the abnormally high temperature in region A and modified the land use type of some pixels from LNDVI to MNDVI, reducing the SUHI levels. Combined with the remote sensing images, most of the modified pixels were located in the connecting areas of different land types, that were originally covered with a certain amount of vegetation. This reduces suitability loss during land conversion and is more in line with the planning strategy. Region B lies

in the building material trading market, where population is quite dynamic. Similarly, the model adjusted the land type around and at the market entrance and exit. Although roofs in the market were not adjusted because of the high suitability of LNDVI, changing building properties, increasing roof greening, and reducing building density will be effective thermal mitigation measures (Roth et al., 2022). Region C is located in the Wuhan Iron and Steel Group, the largest industrial park in Wuhan. The alleviation of the industrial heat island effect has been a significant challenge (Gao et al., 2022; Meng et al., 2022). A large amount of anthropogenic heat released by industrial parks spreads to the surrounding areas, exacerbating the UHI effect (Liu et al., 2021). The

model increased the numbers of MNDVI and HNDVI in region C and “greened” the surrounding areas with strong heat aggregation. Adding “mosaic style” small green spaces in the industrial parks can help alleviate the UHI effect, fully utilizing the exposed surface within the industrial park and could be more effective than centralized large green spaces (Singh et al., 2023). In addition, a combination of cool roofs with mixed green patches in industrial stations can help mitigate industrial heat. Notably, most of the pixels are essentially a mixture of multiple land types at a spatial restriction of 30 m, and optimization means increasing the proportion of corresponding land types, rather than completely converting into them. Therefore, the temperature advection effect caused by land use change is limited and difficult to quantify accurately beyond the current pixel, which was not included in this study.

5. Discussion

5.1. Generalization of inverse S-shaped function fitting LST

The function fitting method is commonly used to determine the threshold of urban-rural LST mutations, particularly in metropolises with fuzzy urban-rural boundaries. Many mathematical approaches, such as the exponential decay and Gaussian function methods, have been applied to determine rural LST differences (Qiao et al., 2019; Yao et al., 2022). However, these methods tend to select specific points as rural regions of reference and are typically subjective.

The S-shaped function introduced in this study illustrates the urban-rural LST attenuation well, and the parameters imply the LST in different urban areas. The two-year fitting results for Wuhan City indicate the changes in the scope and intensity of UHI effect and reflect the rapid expansion of urban built-up areas. An investigation of the generalization of inverse S-shaped function fitting LST in different cities worldwide is interesting and worthwhile. We selected three cities with significant UHI effects: Nanchang, China; Boston, United States; and London, United Kingdom. Based on the Landsat 8 images with clear weather (cloud cover of <1%) in August 2022, the results of fitting the urban-rural LST change trend using the inverse S-shaped function are presented in Fig. 17. The fitting effect of Nanchang is better than those of the two other cities, indicating that urban-rural heat attenuation is more in line with the inverse S-shaped function (Fig. 17a). This finding is reasonable because China's urban-rural structure is more hierarchical than those of the two other cities, with the density of impermeable surfaces gradually decreasing from the urban core to the suburbs and then from the town-country combined zone to the countryside. Related studies have also shown that the UHI effect in major cities in China is evident owing to the gradient construction of urban and rural areas (Hou et al., 2021). The geographical location along the coast of Boston restricts the direction of urban expansion, resulting in a more compact urban structure. This also makes the temperature of Boston's urban core considerably higher than

those of the rural areas, which is captured well by the fitted function parameters (Fig. 17b). As a typical example of counter-urbanization, rural areas in London carry many residential activities, and urban functions are gradually shifting toward rural areas. The narrowing of the gap between urban and rural areas is also reflected in the temperature, and the UHI effect in London is relatively weak within the observation range (40 km buffer zone) as shown in Fig. 17c. Overall, the inverse S-shaped function efficiently captures and explains the characteristics of urban-rural LST changes, but some exceptions should be considered. For example, the edges of some urban agglomerations are interconnected, and a single central buffer zone may be unable to capture urban-rural temperature changes (Hsu et al., 2021). Some cities with well-constructed green infrastructure and a high degree of anti-urbanization have urban temperatures even lower than those in the suburbs, and a true rural reference may not exist (Roth et al., 2022). Intra-urban temperature differences should be more relevant from a sustainability perspective. In addition, the method of fitting LST attenuation is more suitable for seasons and climatic zones with significant UHI effects. Differences in climate may also cause the inverse S-shaped functions to fail. In dry regions (deserts or short vegetation), cities are aerodynamically rougher than the surrounding rural surfaces, resulting in more efficient heat dissipation in urban areas (Manoli et al., 2019).

5.2. Optimization modeling for natural processes

Urban greening is an important means of mitigating the UHI effect; however, the previous literature has focused on the analysis of correlations, such as the relationship between landscape configuration and UHI (Deng et al., 2023; Li et al., 2022b). Only a few studies have focused on specific spatial units in urban greening strategies. This study provides a framework for natural process optimization modeling such as UHI, carbon sink, and ecosystem service processes. Specifically, it comprises three major parts. The first part is the spatial explicitness of optimization algorithms. Heuristic algorithms such as ACO, GA, and PSO are spatially implicit and cannot characterize geospatial land-use evolution. In solving geospatial problems, establishing a mapping relationship between optimization algorithms and geospatial space is necessary. Presenting the MACO used in this study as an example, elements in the optimization algorithm, such as each ant that corresponds to a specific land use pixel, the type of ant that corresponds to the specific land use type, and the entire ant colony, were considered in the land use layout scheme. For optimization operations, the pheromone concentration can be mapped to the land conversion probability, and updating the pheromone concentration can be considered a land-type conversion. In addition, the encoding methods of optimization algorithms (e.g., binary and integer encodings) (Liu et al., 2014), operation units (e.g., land use grids and patches) (Song and Chen, 2018), and operators (e.g., evolution and mutation operators) (Huang and Song, 2019) must be mapped and transformed in accordance with the optimization algorithm used. The

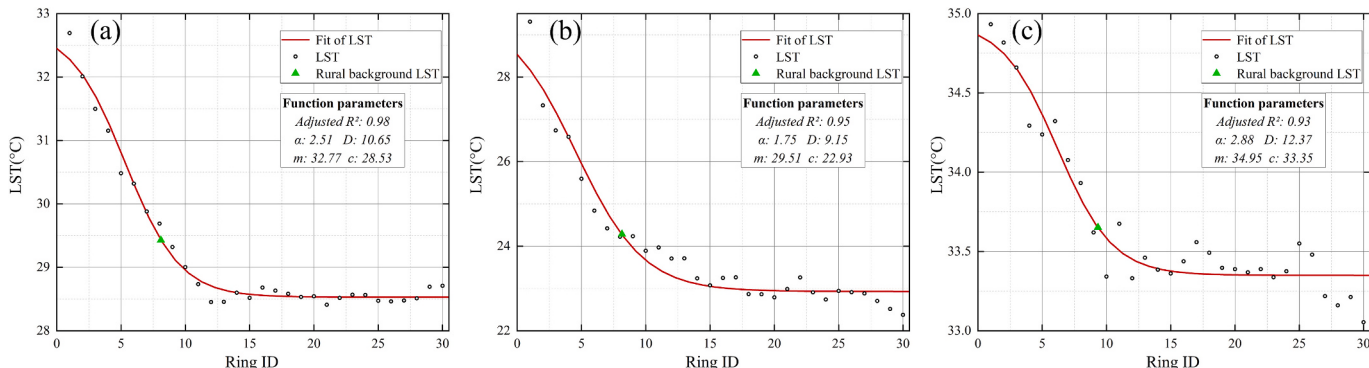


Fig. 17. The fittings of LST using inverse S-shaped function in August 2022 for (a) Nanchang, (b) Boston, and (c) London.

second objective is to establish a matching relationship between natural processes and land use. In this study, the process of LST retrieval was established with respect to land use type, and two key factors for calculating LST (i.e., NDVI and thermal radiation) were estimated. Similarly, when optimizing natural processes such as carbon sinks and ecosystem services, considering how to attach changes in target values to land use transformation is necessary (Li et al., 2023; Zheng et al., 2019). In addition, the strategy of using the global extremum in the iteration and local means in the output of the results is effective when estimating key factors. On the one hand, optimization based on the extremum can ensure faster convergence speed; on the other hand, local means fully consider spatial heterogeneity, making the results more realistic. Third, domain knowledge is integrated into the optimization model. The incorporation of knowledge-informed rules into optimization models to achieve quality solutions for land use layout adjustments has been widely studied by many scholars (Huang and Song, 2019; Liu et al., 2016; Yang et al., 2018). Natural processes are frequently accompanied by certain regularity, and thus, reasonable domain knowledge can avoid redundant searches by changing the structure of the algorithm's search space and preventing random updates of land use to increase the quality of optimization solutions. Compared with classical optimization algorithms, a model incorporating UHI knowledge can focus on the urgency of regional cooling, identify heat core and abnormal areas, and generate more reasonable and desirable solutions in the planning context. Moreover, the spatial distribution of the optimized pixels was more regular, reducing the excessive randomization of traditional optimization models.

5.3. Limitations and future work

The limitations and directions for future work are summarized as follows. The number of cities and seasons selected in this study was relatively small, without spatiotemporal comparison and verification. The analysis of the inverse S-shaped rule in different cities and time points will provide insights into the regional and spatiotemporal variations in the UHI effect. The identified seasonal and recurrent heat islands could inform the formulation of more targeted urban heat mitigation plans, which merit further research (Deng et al., 2023). In addition, scale effects cannot be disregarded in spatial analysis, although this study used only a single-gradient scale buffer. The analysis of LST variation differences and sensitivity under multiscale aggregation may yield more comprehensive conclusions (Xu et al., 2019). Since the cloud content of the remote sensing image affects the accuracy of LST retrieval result, only clear weather was chosen to test the fitting effect, and the sensitivity of the inverse S-shaped function under different weather conditions needs further exploration. Meanwhile, the effectiveness of the inverse S-shaped function in fitting the temperature decay patterns for the multi-center and linear cities can also be explored in the future. Although the proposed optimization model exhibited good performance in cooling urban heat areas while maintaining land-type similarity, the dynamic changes in the UHI process were not fully considered. For example, surface landscape structure may also affect regional LST, and thus, the optimization model can be improved from pixel-based to patch-based to capture patch-level characteristics (e.g., compactness and patch shape). In addition, considering data availability, this study only used quantitative remote sensing indicators to characterize the suitability of different land use configurations. Multiple data sources and indicators can be combined to refine the calculation of the cost and suitability of land use changes in future work. The fairness of cooling facility availability and regional heat vulnerability is important for strengthening urban thermal risk management and planning. The current objectives of the optimization model are relatively single, and multiple objectives, such as fairness and sustainability, can be introduced in subsequent research (Chen et al., 2022).

6. Conclusions

The determination of urban-rural LST differences and cooling the identified SUHI are the main limitations of the related research. With a rapidly expanding urban area, administrative boundaries are difficult to accurately characterize the impact scope of SUHI. Using Landsat 8 image data, we identified the urban boundaries with different impervious surface densities by calculating the ISDD considering spatial distance weight. Combining CCA, the UBMA boundary of Wuhan City was extracted, and the edge of low-density areas was similar to the scope of the Wuhan Urban Development Zone but excluded the cooling areas produced by vegetation and water. Then an inverse S-shaped function was introduced to fit the urban-rural LST attenuation trend. The fitting effect of the proposed function is desirable and the derived parameters with clear physical meanings are useful for describing thermal characteristics, which also avoids subjectivity in the representation of urban-rural LST changes. SUHI at different intensity levels was calculated based on the parameters of the fitted function. By coupling the domain knowledge of the SUHI process and population distribution, a knowledge-informed MACO model was constructed to mitigate the UHI effect. The results showed that the thermal-related knowledge had a direct effect by guiding the greening direction to cool the urban heat areas. The urgency of cooling and the disintegration of the heat core were well reflected in the SUHI mitigation scenarios. The average temperature and the number of residents exposed to high temperatures in the main urban built-up areas decreased significantly after optimization, which could contribute to the improvement and sustainable development of the urban thermal environment. The proposed methods can be easily extrapolated to other metropolises or small cities experiencing the impact of UHI. It could be a useful exploratory tool for urban planners and policymakers to advance the understanding of the SUHI and formulate reasonable urban greening plans. This study also provides guidance and references for urban population thermal health, urban environment, and urban ecological planning. In the context of global warming, our research will help alleviate the UHI effect and improve the livability of cities.

CRediT authorship contribution statement

Zhaomin Tong: Conceptualization, Methodology, Software. **Jiaming Yang:** Data curation, Writing – original draft. **Yaoxin Liu:** Supervision, Writing – review & editing. **Ziyi Zhang:** Visualization, Investigation. **Sui Liu:** Data curation. **Yanchi Lu:** Writing – original draft. **Bowen Pang:** Visualization. **Rui An:** Data curation.

Declaration of competing interest

The authors declare that they have no known competing financial interests or personal relationships that could have appeared to influence the work reported in this paper.

Data availability

Data will be made available on request.

Acknowledgements

This work was supported by the Key Program of National Natural Science Foundation of China (No. 42230107).

Appendix A. Supplementary data

Supplementary data to this article can be found online at <https://doi.org/10.1016/j.rse.2024.114138>.

References

- Athukorala, D., Murayama, Y., 2021. Urban heat island formation in greater Cairo: spatio-temporal analysis of daytime and nighttime land surface temperatures along the urban-rural gradient. *Remote Sens.* 13.
- Chakraborty, T., Hsu, A., Manya, D., Sheriff, G., 2020. A spatially explicit surface urban heat island database for the United States: characterization, uncertainties, and possible applications. *ISPRS J. Photogramm. Remote Sens.* 168, 74–88.
- Chen, X., Zhang, Y., 2017. Impacts of urban surface characteristics on spatiotemporal pattern of land surface temperature in Kunming of China. *Sustain. Cities Soc.* 32, 87–99.
- Chen, M., Jia, W., Yan, L., Du, C., Wang, K., 2022. Quantification and mapping cooling effect and its accessibility of urban parks in an extreme heat event in a megacity. *J. Clean. Prod.* 334.
- Deilami, K., Kamruzzaman, M., Liu, Y., 2018. Urban heat island effect: a systematic review of spatio-temporal factors, data, methods, and mitigation measures. *Int. J. Appl. Earth Obs. Geoinf.* 67, 30–42.
- Deng, C., Wu, C., 2012. BCI: a biophysical composition index for remote sensing of urban environments. *Remote Sens. Environ.* 127, 247–259.
- Deng, X., Gao, F., Liao, S., Liu, Y., Chen, W., 2023. Spatiotemporal evolution patterns of urban heat island and its relationship with urbanization in Guangdong-Hong Kong-Macao greater bay area of China from 2000 to 2020. *Ecol. Indic.* 146.
- Feng, R., Wang, F., Wang, K., Wang, H., Li, L., 2021. Urban ecological land and natural-anthropogenic environment interactively drive surface urban heat island: an urban agglomeration-level study in China. *Environ. Int.* 157, 106857.
- Gao, J., Meng, Q., Zhang, L., Hu, D., 2022. How does the ambient environment respond to the industrial heat island effects? An innovative and comprehensive methodological paradigm for quantifying the varied cooling effects of different landscapes. *GISci. Remote Sens.* 59, 1643–1659.
- Hou, L., Yue, W., Liu, X., 2021. Spatiotemporal patterns and drivers of summer heat island in Beijing-Tianjin-Hebei urban agglomeration, China. *IEEE J. Sel. Top. Appl. Earth Obs. Remote Sens.* 1.
- Hsu, A., Sheriff, G., Chakraborty, T., Manya, D., 2021. Disproportionate exposure to urban heat island intensity across major US cities. *Nat. Commun.* 12, 2721.
- Hu, L., Wilhelmi, O.V., Uejio, C., 2019. Assessment of heat exposure in cities: combining the dynamics of temperature and population. *Sci. Total Environ.* 655, 1–12.
- Huang, Q., Song, W., 2019. A land-use spatial optimum allocation model coupling a multi-agent system with the shuffled frog leaping algorithm. *Comput. Environ. Urban. Syst.* 77.
- Huang, Q., Huang, J., Yang, X., Fang, C., Liang, Y., 2019. Quantifying the seasonal contribution of coupling urban land use types on urban heat island using land contribution index: a case study in Wuhan, China. *Sustain. Cities Soc.* 44, 666–675.
- Jain, S., Sannigrahi, S., Sen, S., Bhatt, S., Chakraborti, S., Rahmat, S., 2020. Urban heat island intensity and its mitigation strategies in the fast-growing urban area. *J. Urban Manag.* 9, 54–66.
- Jiao, L., 2015. Urban land density function: a new method to characterize urban expansion. *Landsc. Urban Plan.* 139, 26–39.
- Kaim, A., Cord, A.F., Volk, M., 2018. A review of multi-criteria optimization techniques for agricultural land use allocation. *Environ. Model Softw.* 105, 79–93.
- Li, X., Parrott, L., 2016. An improved genetic algorithm for spatial optimization of multi-objective and multi-site land use allocation. *Comput. Environ. Urban. Syst.* 59, 184–194.
- Li, H., Zhou, Y., Li, X., Meng, L., Wang, X., Wu, S., Sodoudi, S., 2018. A new method to quantify surface urban heat island intensity. *Sci. Total Environ.* 624, 262–272.
- Li, K., Chen, Y., Wang, M., Gong, A., 2019. Spatial-temporal variations of surface urban heat island intensity induced by different definitions of rural extents in China. *Sci. Total Environ.* 669, 229–247.
- Li, K., Chen, Y., Gao, S., 2022a. Uncertainty of city-based urban heat island intensity across 1112 global cities: background reference and cloud coverage. *Remote Sens. Environ.* 271.
- Li, P., Xu, T., Wei, S., Wang, Z.-H., 2022b. Multi-objective optimization of urban environmental system design using machine learning. *Comput. Environ. Urban. Syst.* 94.
- Li, W., Chen, Z., Li, M., Zhang, H., Li, M., Qiu, X., Zhou, C., 2023. Carbon emission and economic development trade-offs for optimizing land-use allocation in the Yangtze River Delta, China. *Ecol. Indic.* 147.
- Liao, W., Hong, T., Heo, Y., 2021. The effect of spatial heterogeneity in urban morphology on surface urban heat islands. *Energy Build.* 244.
- Liu, X., Li, X., Shi, X., Huang, K., Liu, Y., 2012. A multi-type ant colony optimization (MACO) method for optimal land use allocation in large areas. *Int. J. Geogr. Inf. Sci.* 26, 1325–1343.
- Liu, Y., Yuan, M., He, J., Liu, Y., 2014. Regional land-use allocation with a spatially explicit genetic algorithm. *Landsc. Ecol. Eng.* 11, 209–219.
- Liu, Y., Peng, J., Jiao, L., Liu, Y., 2016. PSOLA: a heuristic land-use allocation model using patch-level operations and knowledge-informed rules. *PLoS One* 11, e0157728.
- Liu, S., Zhang, J., Li, J., Li, Y., Zhang, J., Wu, X., 2021. Simulating and mitigating extreme urban heat island effects in a factory area based on machine learning. *Build. Environ.* 202.
- Liu, Y., Ma, H., Zhang, C., Luo, X., 2022. Watering on porous pavement for improvement of environmental human thermal comfort in an ecological community in arid area: a case study in Lanzhou, China. *Sustain. Cities Soc.* 85.
- Manoli, G., Faticchi, S., Schlapfer, M., Yu, K., Crowther, T.W., Meili, N., Burlando, P., Katul, G.G., Bou-Zeid, E., 2019. Magnitude of urban heat islands largely explained by climate and population. *Nature* 573, 55–60.
- Meng, Q., Zhang, L., Sun, Z., Meng, F., Wang, L., Sun, Y., 2018. Characterizing spatial and temporal trends of surface urban heat island effect in an urban main built-up area: a 12-year case study in Beijing, China. *Remote Sens. Environ.* 204, 826–837.
- Meng, Q., Hu, D., Zhang, Y., Chen, X., Zhang, L., Wang, Z., 2022. Do industrial parks generate intra-heat island effects in cities? New evidence, quantitative methods, and contributing factors from a spatiotemporal analysis of top steel plants in China. *Environ. Pollut.* 292, 118383.
- Mohammad, P., Goswami, A., 2022. Exploring different indicators for quantifying surface urban heat and cool island together: a case study over two metropolitan cities of India. *Environ. Dev. Sustain.* 25, 10857–10878.
- National Climate Center of China Meteorological Administration, 2022. China Climate Bulletin 2022. <http://www.ncc-cma.net/channel/news/newsid/100060>.
- Nguyen, C.T., Chidthaisong, A., Limsakul, A., Varnakovida, P., Ekkawatpanit, C., Diem, P.K., Diep, N.T.H., 2022. How do disparate urbanization and climate change imprint on urban thermal variations? A comparison between two dynamic cities in Southeast Asia. *Sustain. Cities Soc.* 82.
- Pena Acosta, M., Vahdatkhaki, F., Santos, J., Hammad, A., Dorée, A.G., 2021. How to bring UHI to the urban planning table? A data-driven modeling approach. *Sustain. Cities Soc.* 71.
- Peng, J., Dan, Y., Qiao, R., Liu, Y., Dong, J., Wu, J., 2021. How to quantify the cooling effect of urban parks? Linking maximum and accumulation perspectives. *Remote Sens. Environ.* 252.
- Possega, M., Aragão, L., Ruggieri, P., Santo, M.A., Di Sabatino, S., 2022. Observational evidence of intensified nocturnal urban heat island during heatwaves in European cities. *Environ. Res. Lett.* 17.
- Qian, J., Meng, Q., Zhang, L., Schlink, U., Hu, X., Gao, J., 2023. Characteristics of anthropogenic heat with different modeling ideas and its driving effect on urban heat islands in seven typical Chinese cities. *Sci. Total Environ.* 886, 163989.
- Qiao, Z., Wu, C., Zhao, D., Xu, X., Yang, J., Feng, L., Sun, Z., Liu, L., 2019. Determining the boundary and probability of surface urban heat island footprint based on a logistic model. *Remote Sens.* 11.
- Rahman, M.M., Szabó, G., 2021. Multi-objective urban land use optimization using spatial data: a systematic review. *Sustain. Cities Soc.* 74.
- Rakoto, P.Y., Deilami, K., Hurley, J., Amati, M., Sun, Q., 2021. Revisiting the cooling effects of urban greening: planning implications of vegetation types and spatial configuration. *Urban For. Urban Green.* 64.
- Roth, M., Sanchez, B., Li, R., Velasco, E., 2022. Spatial and temporal characteristics of near-surface air temperature across local climate zones in a tropical city. *Int. J. Climatol.* 42, 9730–9752.
- Rosenfeld, H.D., Rybski, D., Andrade Jr., J.S., Batty, M., Stanley, H.E., Makse, H.A., 2008. Laws of population growth. *Proc. Natl. Acad. Sci. USA* 105, 18702–18707.
- Schwarz, N., Lautenbach, S., Seppelt, R., 2011. Exploring indicators for quantifying surface urban heat islands of European cities with MODIS land surface temperatures. *Remote Sens. Environ.* 115, 3175–3186.
- Shen, H.F., Huang, L.W., Zhang, L.P., Wu, P.H., Zeng, C., 2016. Long-term and fine-scale satellite monitoring of the urban heat island effect by the fusion of multi-temporal and multi-sensor remote sensed data: a 26-year case study of the city of Wuhan in China. *Remote Sens. Environ.* 172, 109–125.
- Sheng, S., Xiao, H., Wang, Y., 2022. The cooling effects of hybrid landscapes at the district scale in mega-cities: a case study of Shanghai. *J. Clean. Prod.* 366.
- Singh, V.K., Mohan, M., Bhati, S., 2023. Industrial heat island mitigation in Angul-Talcher region of India: evaluation using modified WRF-single urban canopy model. *Sci. Total Environ.* 858, 159949.
- Sobrino, J.A., Jimenez-Munoz, J.C., Soria, G., Romaguera, M., Guanter, L., Moreno, J., Plaza, A., Martinez, P., 2008. Land surface emissivity retrieval from different VNIR and TIR sensors. *IEEE Trans. Geosci. Remote Sens.* 46, 316–327.
- Song, M., Chen, D., 2018. An improved knowledge-informed NSGA-II for multi-objective land allocation (MOLA). *Geo-spat. Inf. Sci.* 21, 273–287.
- Sugg, M.M., Runkle, J.D., Dow, K., Barnes, J., Stevens, S., Pearce, J., Bossak, B., Curtis, S., 2022. Individually experienced heat index in a coastal southeastern US city among an occupationally exposed population. *Int. J. Biometeorol.* 66, 1665–1681.
- Sun, Y., Gao, C., Li, J., Wang, R., Liu, J., 2019. Evaluating urban heat island intensity and its associated determinants of towns and cities continuum in the Yangtze River Delta urban agglomerations. *Sustain. Cities Soc.* 50.
- Tong, Z., Zhu, Y., Zhang, Z., An, R., Liu, Y., Zheng, M., 2022. Unravel the spatio-temporal patterns and their nonlinear relationship with correlates of dockless shared bikes near metro stations. *Geo-spat. Inf. Sci.* 1–22.
- UN-Habitat, 2022. World Cities Report 2022: Envisaging the Future of Cities. https://unhabitat.org/sites/default/files/2022/06/wcr_2022.pdf.
- Walawender, J.P., Szymonowski, M., Hajto, M.J., Bokwa, A., 2013. Land surface temperature patterns in the urban agglomeration of Krakow (Poland) derived from Landsat-7/ETM+ data. *Pure Appl. Geophys.* 171, 913–940.
- Wang, W., Jiao, L., Jia, Q., Liu, J., Mao, W., Xu, Z., Li, W., 2021a. Land use optimization modelling with ecological priority perspective for large-scale spatial planning. *Sustain. Cities Soc.* 65.
- Wang, Z., Meng, Q., Allam, M., Hu, D., Zhang, L., Menenti, M., 2021b. Environmental and anthropogenic drivers of surface urban heat island intensity: a case-study in the Yangtze River Delta, China. *Ecol. Indic.* 128.
- Wang, H., Li, B., Yi, T., Wu, J., 2022a. Heterogeneous urban thermal contribution of functional construction land zones: a case study in Shenzhen, China. *Remote Sens.* 14.
- Wang, Y., Li, X., Zhang, C., He, W., 2022b. Influence of spatiotemporal changes of impervious surface on the urban thermal environment: a case of Huai'an central urban area. *Sustain. Cities Soc.* 79.

- Wang, Q., Wang, X., Meng, Y., Zhou, Y., Wang, H., 2023. Exploring the impact of urban features on the spatial variation of land surface temperature within the diurnal cycle. *Sustain. Cities Soc.* 91.
- Welegedara, N.P.Y., Agrawal, S.K., Lotfi, G., 2023. Exploring spatiotemporal changes of the urban heat island effect in high-latitude cities at a neighbourhood level: a case of Edmonton, Canada. *Sustain. Cities Soc.* 90.
- Xing, L., Liu, Y., Wang, B., Wang, Y., Liu, H., 2020. An environmental justice study on spatial access to parks for youth by using an improved 2SFCA method in Wuhan, China. *Cities* 96.
- Xu, G., Dong, T., Cobbina, P.B., Jiao, L., Sumari, N.S., Chai, B., Liu, Y., 2019. Urban expansion and form changes across African cities with a global outlook: spatiotemporal analysis of urban land densities. *J. Clean. Prod.* 224, 802–810.
- Xue, X., He, T., Xu, L., Tong, C., Ye, Y., Liu, H., Xu, D., Zheng, X., 2022. Quantifying the spatial pattern of urban heat islands and the associated cooling effect of blue-green landscapes using multisource remote sensing data. *Sci. Total Environ.* 843, 156829.
- Yang, L., Cao, Y., Zhu, X., Zeng, S., Yang, G., He, J., Yang, X., 2014. Land surface temperature retrieval for arid regions based on Landsat-8 TIRS data: a case study in Shihezi, Northwest China. *J. Arid. Land* 6, 704–716.
- Yang, L., Zhu, A., Shao, J., Chi, T., 2018. A knowledge-informed and Pareto-based artificial bee colony optimization algorithm for multi-objective land-use allocation. *ISPRS Int. J. Geo Inf.* 7.
- Yao, R., Wang, L., Huang, X., Niu, Y., Chen, Y., Niu, Z., 2018. The influence of different data and method on estimating the surface urban heat island intensity. *Ecol. Indic.* 89, 45–55.
- Yao, L., Sun, S., Song, C., Wang, Y., Xu, Y., 2022. Recognizing surface urban heat 'island' effect and its urbanization association in terms of intensity, footprint, and capacity: a case study with multi-dimensional analysis in northern China. *J. Clean. Prod.* 372.
- Yu, X., Guo, X., Wu, Z., 2014. Land surface temperature retrieval from Landsat 8 TIRS—comparison between radiative transfer equation-based method, split window algorithm and single channel method. *Remote Sens.* 6, 9829–9852.
- Yu, Z., Yang, G., Zuo, S., Jørgensen, G., Koga, M., Vejre, H., 2020. Critical review on the cooling effect of urban blue-green space: a threshold-size perspective. *Urban For. Urban Green.* 49.
- Zhang, Y., Chen, X., Lv, D., Zhang, Y., 2021. Optimization of urban heat effect mitigation based on multi-type ant colony algorithm. *Appl. Soft Comput.* 112.
- Zhang, Y., Wang, J., Kan, C., 2022. Temporal variation in activity-space-based segregation: a case study of Beijing using location-based service data. *J. Transp. Geogr.* 98.
- Zheng, W., Ke, X., Xiao, B., Zhou, T., 2019. Optimising land use allocation to balance ecosystem services and economic benefits - a case study in Wuhan, China. *J. Environ. Manag.* 248, 109306.
- Zhou, Y., Zhao, H., Mao, S., Zhang, G., Jin, Y., Luo, Y., Huo, W., Pan, Z., An, P., Lun, F., 2022. Exploring surface urban heat island (SUHI) intensity and its implications based on urban 3D neighborhood metrics: an investigation of 57 Chinese cities. *Sci. Total Environ.* 847, 157662.